Local Phasor-Based Control on Three-phase Radial Distribution Networks

Jaimie Swartz

Electrical Engineering and Computer Sciences
University of California, Berkeley

Technical Report No. UCB/EECS-2021-206
http://www2.eecs.berkeley.edu/Pubs/TechRpts/2021/EECS-2021-206.html

August 24, 2021

Local Phasor-Based Control on Three-phase Radial Distribution Networks

by

Jaimie Swartz

A dissertation submitted in partial satisfaction of the

requirements for the degree of

Master of Science

in

Electrical Engineering and Computer Science

in the

Graduate Division

of the

University of California, Berkeley

Committee in charge:

Professor Claire Tomlin, Co-chair, Chair
Adjunct Professor Alexandra von Meier, Co-chair
Professor Duncan Callaway
Professor Seth Sanders

Spring 2021

Local Phasor-Based Control on Three-phase Radial Distribution Networks

To my family, my adviser Sascha, and the ENERGISE team.

Contents

List of Figures

List of Tables

Chapter 1

Introduction

1.1 Distributed Energy Resource Control

To reduce carbon emissions and dependence on fossil fuels for energy production, many countries are dramatically increasing electric power generation from renewable, variable, and distributed resources. Other cost-effective technologies such as all-electric vehicles, automated demand response and customer- or community-scale energy storage are experiencing significant growth. These distributed energy resources (DERs) introduce both challenges and opportunities. Specific issues of concern with residential-scale solar photovoltaics (PV) include overvoltage which can reduce the lifespan of grid equipment as well as protection issues such as relay desensitization and protection zone malfunctions due to reverse power flow [4–6]. Additionally, solar variability can ramp up on the order of 15% of its capacity per minute [7] and lead to network congestion at times of peak demand [8]. For these reasons, distribution utilities may limit the connection (or permissible levels) of PV generation by defining feeder hosting capacities. Electric vehicle charging, if not carefully controlled, may similarly strain the limits of legacy distribution systems [9].

In traditional volt/var control (VVC), voltage regulating devices such as capacitors and load tap changers are supposed to maintain distribution grid voltage to within the ASCI standard [10] but they are not designed to these highly variable solar generation fluctuations. As a result these devices may operate continuously, which deteriorates their operating life [11, 12].

The PV and battery inverters have emerged as an effective solutions to handle rapid variations in the modern distribution system. In addition to converting the DC to AC power, smart inverters have the capability to inject real and/or reactive power into the grid based on the inverter control settings and availability of the PV or battery resource. In fact, the 2018 smart inverter IEEE 1547 standard [13] requires that inverters have reactive power support capabilities and, in areas with high penetration, real power support as well. Additionally, policies are developing that incentivize aggregated DERs to provide power and services for transmission-level markets. However, in doing so these resources may create local problems at the distribution level: for example, causing voltage volatility while providing frequency regulation services to the bulk grid. Thus optimizing on a larger geographic scale should be accompanied by local or distributed control layers that take actions quickly and account for the take into account the highly location-specific constraints of distribution networks that must be satisfied. To support the cost-effective integration of controllable DERs that not only combat the variability of uncontrollable resources but also improve the delivery of reliable, high-quality power, more sophisticated approaches for controlling heterogeneous DERs are needed [14–17].

1.2 Phasor-measurement Units (PMUs)

Sophisticated approaches for controlling DERs require advanced sensing capabilities. Phasor-measurement units (PMUs) are devices that have been successfully used to measure the voltage magnitude and phase angle of the electricity grid using GPS synchronization. As a result, the number of installments of PMUs on transmission grids has grown dramatically in recent years [18]. One important type of PMU is ultra-precise synchronized phasor measurement units (μPMUs), which provide synchrophasor data with sufficient resolution for the power distribution context. These instruments can reliably discern angle differences as small as ten millidegrees, or about half a microsecond [19].

1.3 Phasor-Based Control

The recent development of μPMUs enables the opportunity to implement Phasor-Based Control (PBC). The PBC framework is designed to facilitate the integration of heterogeneous and intermittent distributed energy resources (DER) on the electric grid. PBC presents a unified approach that is agnostic to optimization criteria and to the particular characteristics of participating resources. Further, it can be deployed across transmission and distribution level grids. At its core, PBC frames the control of DERs around meeting voltage phasor references,as opposed to power (real and/or reactive) references. By designing controllers around the physical grid quantity of voltage, there are opportunities to improve the power quality and stability of the grid.

Phasor-based control employs a multi-layer control hierarchy that decouples high level long-term optimal objectives from short-term power quality objectives [20]. There exists a centralized controller (called S-PBC) that solves an optimal power flow (OPF) problem periodically to determine optimal voltage phasor targets. The OPF objectives that can be specified by a utility or other external operator. Some objectives can be very effectively expressed in terms of target voltage phasors at specific nodes, including reducing voltage volatility, balancing three phases, preventing reverse power flow on distribution circuits, and matching voltage phasors across an open switch for topology changes (such as flexible restoration or microgrid islanding). The phasor targets computed by the S-PBC are broadcast across a network to one or more feedback controllers. Each controller computes a set of real and reactive power setpoint commands for one or more controllable resources so that the resources drive the voltage phasors to their targets. When the phasor targets are met, the objectives defined in the OPF formulation are achieved.

The PBC system is agnostic to the optimization formulation, the characteristics of participating resources, and the structure of the grid. PBC frames the contributions of generators and loads in terms of their physical effect on the network, by explicitly referring to the electrical state variables, voltage magnitude and voltage phase angle, that constitute the voltage *phasor* at any given network node, not only nodes with DER. The use of the phasor as a network state variable enables an immediate corrective response to disturbances without communication between L-PBCs nor between resources without compromising privacy.

PBC in Relation to Other Literature

Inverter control strategies for microgrids (AC or DC low voltage distribution networks) range from centralized to completed decentralized. Some strategies proposed fall into a three-layer hierarchical control architecture [21–23]. A diagram of this architecture is in Fig. 1.1. In this framework, the primary control layer is comprised of outer droop frequency-watt and droop volt-var loops, as well as inner current and voltage loops that determine the switching sequence of the physical inverter circuit. The secondary layer is designed to remove deviations in global frequency and local voltage from nominal values that tend to be caused by the droop operations. This removal function improves the power sharing between inverters. The tertiary layer is concerned with global economic dispatch and factors in electricity market prices. The S-PBC is comparable to the tertiary layer, but instead of outputting real power references the S-PBC outputs optimal voltage phasor references. The L-PBC is most comparable to the combination of the outer droop control portion of the primary layer and the secondary layer. That is, instead of tracking voltage magnitude references with reactive power and frequency references with real power, L-PBC tracks voltage magnitude and phase references with real and reactive power commands without necessarily needing a layer to remove voltage or frequency deviations.

In recent years there has been discussion about grid forming and grid-following inverters, especially in the context of microgrid stability [24, 25]. The distinction between grid-forming and grid following inverters centers around whether the grid frequency is estimated from the measured voltage using a PLL (grid-following) or set as the nominal frequency to be produced by the inverter (grid-forming). These terms specify the architecture associated with the inner current and voltage control loops, which is below the power setpoint control loops. Because L-PBC is associated with the inverter power setpoint loops and the secondary control layer, PBC can be incorporated into both grid-forming and grid-following inverters.

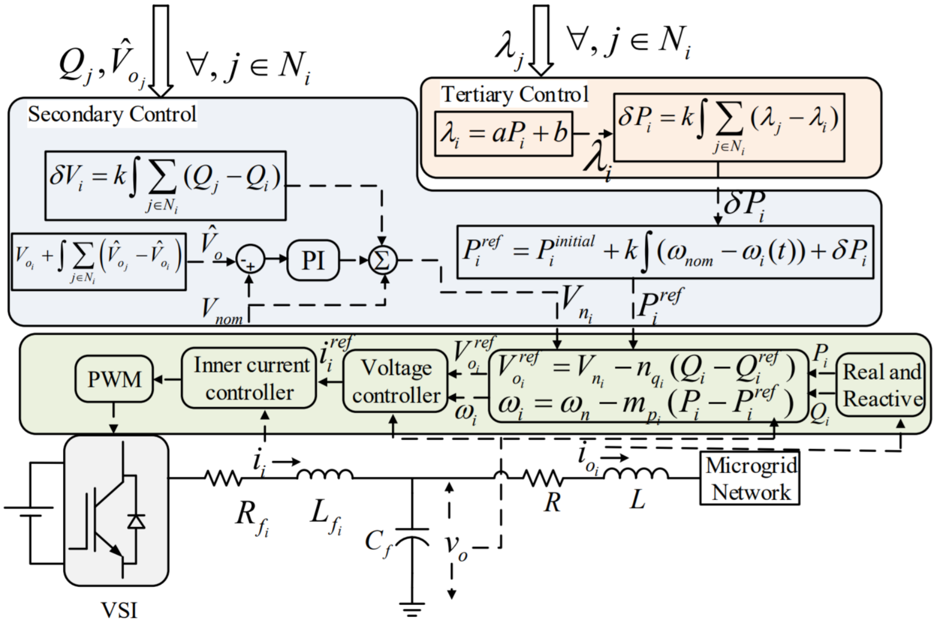

Figure 1.1: Hierarchical control diagram for inverter i of an AC microgrid from [1].

Table 1.1: Notation for the diagram of Fig. 1.1.

ω_{nom}	nominal inverter frequency
ω	frequency
α	phase angle
P	inverter outputted real power
P^{ref}	real power reference
Q	inverter outputted reactive power
Q^{ref}	reactive power reference
V_o	inverter terminal voltage magnitude
V_o^{ref}	reference voltage magnitude
λ	marginal cost factor
δP	average marginal cost consensus
δV	average reactive power consensus
$\hat{V}_o$	average voltage consensus
n_q	volt-var droop gain
m_p	frequency-watt droop gain
i^{ref}	terminal current reference

1.4 Thesis Abstract

In this thesis we explore the modeling, design, and implementation of Phasor-Based Control (PBC), where DERs are coordinated to achieve power quality objectives on 3-phase distribution networks. Drawing inspiration from control theory and practical limitations in power systems, we address challenges associated with controlling real and reactive power to achieve voltage phasor target tracking goals. We focus on the local control layer of PBC, called L-PBC. The goal of designing the L-PBC is to determine appropriate feedback control strategies so that computed inverter power setpoints will result in effective phasor tracking. To achieve this, we examine the design of feedback controller parameters, the hardware implementation of PBC, and the placement of L-PBC actuators and sensors.

We begin with Chapter 2, which describes relevant background information, including a power flow linearization that admits power-voltage sensitivity relationships. We show one measurement-based method for estimating these sensitivities on real grids. We also describe a few types of simulations applied to power systems in order to identify the type of analysis we adopt in this thesis.

In Chapter 3 we propose a feedback control law and tuning method for designing the L-PBC. Specifically, we employ a Proportional-Integral (PI) control law that computes real and reactive power setpoints of inverter-based DERs to simultaneously track a phasor target. The measurement-based method described in Chapter 2 is employed to obtain power-voltage sensitivities. We then use a genetic algorithm to tune candidate control parameters based on the steady-state closed-loop response of model on each phase at each node in the grid. Through simulation on the IEEE 13-node grid, we demonstrate that the proposed tuning method yields better performance than the Ziegler Nichols PI controller tuning method. We also observe improved voltage regulation in high PV penetration simulations when compared to droop volt-var control (DVVC). Finally, when simulating on larger grids, we observe more oscillatory closed-loop performance that motivates further investigation.

In Chapter 4, we describe the hardware implementation of the control law and tuning algorithm presented in Chapter 3. The testbed, located at Lawrence Berkeley National Lab, includes smart inverters connected to battery storage and solar photovoltaics, controllable loads, and a μPMU sensor. To run hardware-in-the-loop (HIL) testing, we setup a cyber-physical system, in which measurements to and from real devices are spatially integrated onto a virtual distribution grid. We also perform controller-in-the-loop (CIL) tests, which is an intermediate setup between software simulations and HIL testing. The hardware tests exhibit effective rejection of virtual disturbances created by large variations in solar and load profiles. For four of the most critical tests, we compare the performance of the L-PBC control between software simulations, CIL tests, and HIL tests.

In Chapter 5, more complex configurations of inverters and sensors are investigated for applications on larger distribution grids. To do so, the integrator part of the control law proposed in Chapter 3 and the linearized power flow equations are formalized into a linear time-invariant model. This enables the use of eigenvalue stability analysis to evaluate whether a sampled set of controller gains yields phasor tracking of all actuator-sensor control pairs on the grid. By incorporating the stability analysis into a tool that cycles through many possible configurations, we determine topological properties of large feeders that contribute to or inhibit stable controller configurations.

Chapter 2

Background

This chapter outlines background that will be used in this thesis. It acts as a primer for those less familiar with power systems and certain topics in distribution grid management. This chapter can be skipped without loss of continuity, with sections being referred to in the later chapters.

2.1 Power Flow Linearization

Notation: Let $\mathcal{N} = \{0, 1, 2, ..., n\}$ be the set of nodes (buses), with node 0 representing the substation node (slack bus), and $\mathcal{L} \subset \mathcal{N} \times \mathcal{N}$ be the set of lines connecting these nodes. That is, for each pair of nodes $i, j \in \mathcal{N}$, there is a line connecting them iff $(i, j) \in \mathcal{L}$. The complex impedance of line (i, j) is given by $z_{ij} = r_{ij} + \mathbf{j}x_{ij}$, where $\mathbf{j} = \sqrt{-1}$. The complex power flowing from node i to node j is given by $P_{ij} + \mathbf{j}Q_{ij}$. Let the net power injection at node i be $p_i + \mathbf{j}q_i$, and the voltage magnitude at node i be V_i. The the Distflow [26] branch equations for a single-phase radial network can be formulated as

$$P_{ij} = \sum_{k:(i,k)\in\mathcal{L}} P_{jk} - p_j + r_{ij}\frac{(P_{ij}^2 + Q_{ij}^2)}{|V_j|^2} \tag{2.1}$$

$$Q_{ij} = \sum_{k:(i,k)\in\mathcal{L}} Q_{jk} - q_j + x_{ij}\frac{(P_{ij}^2 + Q_{ij}^2)}{|V_j|^2} \tag{2.2}$$

$$V_i^2 - V_j^2 = 2(r_{ij}P_{ij} + x_{ij}Q_{ij}) + (r_{ij}^2 + x_{ij}^2)\frac{(P_{ij}^2 + Q_{ij}^2)}{V_j^2} \tag{2.3}$$

$$\forall (i, j) \in \mathcal{L} \tag{2.4}$$

The linearization of these power flow equations about the nominal voltage of $1p.u.$, called Simplified DistFlow [26], involves approximating the current as zero, that is $I_{ij} = \frac{P_{ij}^2 + Q_{ij}}{V_i^2} \approx 0$. The linearization of equation (2.3) gives

$$V_i^2 - V_j^2 \approx 2(r_{ij}P_{ij} + x_{ij}Q_{ij}) \tag{2.5}$$

The relationship between nodal voltage phase angles δ_i, δ_j and power flow on a single-phase radial network is described by

$$\sin(\delta_i - \delta_j) = \frac{x_{ij}P_{ij} - r_{ij}Q_{ij}}{V_iV_j} \qquad \forall(i,j) \in \mathcal{L} \tag{2.6}$$

To linearize the equation, we make the small-angle approximation $\sin\delta \approx \delta$ and assume $V_i \approx V_j \approx 1p.u.$, retaining the dependence of P_{ij} and Q_{ij} on $(\delta_i - \delta_j)$ [20].

$$\delta_i - \delta_j \approx \frac{x_{ij}P_{ij} - r_{ij}Q_{ij}}{V_iV_j}, \tag{2.7}$$

Note that δ_i in (2.6) and (2.7) can be measured by a UPMU by comparing the voltage waveform at node i, $v_i(t) = V_i^{max}\cos(\omega t + \delta_i)$, to that of a reference node $v_{ref}(t) = V^{max}\cos(\omega t)$ which is typically chosen as the distribution substation node. ω is the (assumed to be constant) waveform angular frequency equal to $2\pi 50$ or $2\pi 60$. For the phasor notation $V_{max}e^{j\delta} = V\angle\delta$, where $V = \frac{1}{\sqrt{2}}V_{max}$ is the root-mean-square magnitude. Equations (2.5) and (2.7) along with the ability to measure the full voltage phasor motivates the controlling of voltage phasors while rejecting steady-state disturbances and disturbances that are on the order of $1Hz$ or slower.

Sensitivities

For a grid network with only PQ buses and one slack bus, the power flow jacobian is defined by

$$\begin{bmatrix}\Delta\mathbf{q}\\ \Delta\mathbf{p}\end{bmatrix} = J\begin{bmatrix}\Delta\mathbf{v}\\ \Delta\boldsymbol{\delta}\end{bmatrix}, \quad J = \begin{bmatrix}\frac{\partial\mathbf{q}}{\partial\mathbf{v}} & \frac{\partial\mathbf{q}}{\partial\delta}\\ \frac{\partial\mathbf{p}}{\partial\mathbf{v}} & \frac{\partial\mathbf{p}}{\partial\boldsymbol{\delta}}\end{bmatrix} \tag{2.8}$$

where v_i is the squared voltage magnitude at bus i, δ_i the voltage phase angle with respect to the reference at the substation node, p_i the net real power, q_i the net reactive power. Then define vectors $\mathbf{v} = [v_1, v_2, ...v_n]^T$, $\boldsymbol{\delta} = [\delta_1, \delta_2, ...\delta_n]^T$, $\mathbf{p} = [p_1, p_2, ...p_n]^T$, and $\mathbf{q} = [q_1, q_2, ...q_n]^T$ on a network with n nodes [27, Chapter 6.4.3]. The jacobian represents the small-signal mapping of voltage phasors to real and reactive power flows near the linearization point.

In transmission systems, where inductive reactance is generally much greater than resistance, reactive power varies mainly with the voltage magnitude, while real power varies mainly with voltage phase angle. That is, a decoupling assumption of $\frac{\partial\mathbf{q}}{\partial\boldsymbol{\delta}} \approx 0$ and $\frac{\partial\mathbf{p}}{\partial\mathbf{v}} \approx 0$ is often. However, distribution feeders tend to have significant resistive components, and consequently real and reactive power is intertwined with both voltage magnitude and phase angle. Moreover, for designing controllers that inject power to regulate voltage on distribution grids, it is useful to determine all four blocks of the inverse mapping matrix H, which is often referred to as a sensitivity matrix.

$$\begin{bmatrix}\Delta\mathbf{v}\\ \Delta\boldsymbol{\delta}\end{bmatrix} = H\begin{bmatrix}\Delta\mathbf{q}\\ \Delta\mathbf{p}\end{bmatrix}, \quad H = \begin{bmatrix}\frac{\partial\mathbf{v}}{\partial\mathbf{q}} & \frac{\partial\mathbf{v}}{\partial\mathbf{p}}\\ \frac{\partial\boldsymbol{\delta}}{\partial\mathbf{q}} & \frac{\partial\boldsymbol{\delta}}{\partial\mathbf{p}}\end{bmatrix} \tag{2.9}$$

To determine H, one could use grid impedance information. However, because distribution grid impedance models are often incomplete or inaccurate, there are works that explore model-less methods for computing H through measurements of different types and configurations of sensors [28, 29]. In what follows, we show a measurement-based method based on power injection step responses that (1) is employed in Chapter 3 for designing PBC controllers, and (2) makes clear the direct relationship between H and grid impedances.

Consider the linearized power flow equations for a 2-bus network with slack bus at node 0, PQ bus at node 1, and line $r + \mathbf{j}x$. For this two bus system, a nodal power injection at the PQ bus $p + \mathbf{j}q$ is equal to the line power. We consider these equations at an initial time k_0 and the next steady state time k_{ss}, with a power injection that occurs between these times. We assume the injection is small enough to assume the PQ bus voltage at both timesteps remains near the linearization point of $1 p.u.$. That is, $V_1^0 \approx V_1^{ss} approx 1$. Together with the slack bus having $V_0^0 = V_0^{ss} = 1$, equations (2.5) and (2.7) becomes

$$(V_1^0)^2 - (V_0^0)^2 = 2rp^0 + 2xq^0 \tag{2.10}$$

$$(\delta_2^0)^2 - (\delta_1^0)^2 = xp^0 - rq^0 \tag{2.11}$$

$$(V_1^{ss})^2 - (V_0^{ss})^2 = 2rp^{ss} + 2xq^{ss} \tag{2.12}$$

$$(\delta_2^{ss})^2 - (\delta_1^{ss})^2 = xp^{ss} - rq^{ss} \tag{2.13}$$

Subtracting equation (2.10) from (2.12) and rearranging gives

$$((V_1^{ss})^2 - (V_1^0)^2) - ((V_0^{ss})^2 - (V_0^0)^2) = 2r(p^{ss} - p^0) + 2x(q^{ss} - q^0) \tag{2.14}$$

$$\frac{(V_1^{ss})^2 - (V_1^0)^2}{q^{ss} - q^0} - \frac{(V_0^{ss})^2 - (V_0^0)^2}{q^{ss} - q^0} = \frac{2r(p^{ss} - p^0)}{q^{ss} - q^0} + 2x \tag{2.15}$$

Because node 1 is a slack bus, $V_0^{ss} = V_0^0$. If a small step change in reactive power is injected at node 2 between k_0 and k_{ss} and there is no change in real power ($p^{ss} - p^0 = 0$), we have

$$\frac{\partial \mathbf{v}}{\partial \mathbf{q}} \approx \frac{(V_1^{ss})^2 - (V_1^0)^2}{q^{ss} - q^0} = 2x \tag{2.16}$$

If instead a step change in only real power is applied, we have

$$\frac{\partial \mathbf{v}}{\partial \mathbf{p}} \approx \frac{(V_1^{ss})^2 - (V_1^0)^2}{p^{ss} - p^0} = 2r \tag{2.17}$$

Subtracting equation (2.11) from (2.13) and rearranging gives

$$((\delta_2^{ss})^2 - (\delta_2^0)^2) - ((\delta_1^{ss})^2 - (\delta_1^0)^2) = x(p^{ss} - p^0) - r(q^{ss} - q^0) \tag{2.18}$$

$$\frac{(\delta_2^{ss})^2 - (\delta_2^0)^2}{p^{ss} - p^0} - \frac{(\delta_1^{ss})^2 - (\delta_1^0)^2}{p^{ss} - p^0} = -\frac{r(q^{ss} - q^0)}{p^{ss} - p^0} + x \tag{2.19}$$

If a step change in reactive power is injected at node 2 between k_0 and k_{ss} we have

$$\frac{\partial \boldsymbol{\delta}}{\partial \mathbf{p}} \approx \frac{(\delta_1^{ss})^2 - (\delta_1^0)^2}{p^{ss} - p^0} = x \tag{2.20}$$

If instead a step change in only reactive power is applied, we have

$$\frac{\partial \boldsymbol{\delta}}{\partial \mathbf{p}} \approx \frac{(\delta_1^{ss})^2 - (\delta_1^0)^2}{q^{ss} - q^0} = r \tag{2.21}$$

These relationships have been validated numerically on several nodes of the IEEE 13-node feeder using the power flow solver ePHASORSIM. When a network has more than two nodes, by choosing V_0 as the slack bus, the impedances obtained from the relationships four relationships eqs. (2.16), (2.17), (2.20) and (2.21) is the effective impedance between the node of interest and the slack bus. Using these relationships, we can create use measurements from step changes in power that are near the linearization point to approximate impedance values. This method can help improve distribution models and, as will be shown in Chapter 3, provides model information for inverter control design.

2.2 Types of Grid Simulations

In this section we describe two types of simulation methods commonly applied to distribution grids in order to make clear the framing of our work.

In quasi-static-time-series (QSTS) simulations, each timestep of QSTS simulations, which are typically between one second and one hour, represents the steady state of the system. These steady states are computed by solving algebraic power flow equations at each timestep, and the inputs to each power flow computation are determined by discrete events. The key distinction between QSTS and dynamic simulations is that QSTS simulations do not involve solving differential equations. Rather, QSTS simulations hinge on the assumption that dynamic transients between discrete timesteps are stable and settle to a steady state. QSTS simulations can provide insights on the interaction of many slow-acting grid components on large-scale grid systems. For example, one could incorporate schedules of loads and uncontrollable renewable generation to see whether voltage regulation devices can mitigate voltage violations [30]. Note that voltage regulation devices in QSTS simulations can have a set schedule of operation or a static relationship to voltage levels. Until converter-based generation with its fast-acting dynamic was widely deployed, many distribution system simulations were of the QSTS type.

In Differential-Algebraic Equation (DAE) simulations, we gather differential equations $\dot{x} = f(x, y)$ and algebraic equations $0 = g(x, y)$ into a system. The system simulation is propagated forward by numerical integration between short timesteps, typically between 1ms and 1s for power systems applications. For example, when a synchronous generator is connected with a line to an infinite bus, one could setup a DAE simulation that incorporate the generator's power-frequency dynamics with the power flow along the line. DAE simulations have also become popular for assessing small-signal stability and dynamic interactions in low-inertia grids, as done in [24, 31–33].

One technique for simplifying DAEs is to linearize the power flow equations, which we make use of in this work. That way, instead of solving power flow regularly during simulation, the power flow linearization (like in (2.5)) can simply be forward-evaluated to obtain grid voltages. This may allow the DAE system to become a purely dynamic system, which could be easier to simulate and analyze. Another technique to simplify DAE analysis is to model device dynamics of only a certain timescale, often the slower ones. That is, faster-acting dynamics are assumed to settle to steady state and are not considered in the stability analysis. This set of assumptions have been used to evaluate inverter power-voltage setpoint control laws by modeling them in a quasi-steady state dynamical system. For example, works of [34–38] analyze droop volt-var controlled inverters by choosing the simulation timestep to be large enough for the inverter's lower level control loops to reach the power setpoint dictated by the droop curve. Our work includes this assumptions to evaluate power-voltage setpoint control laws as well.

Common software used for distribution grid simulations include GridLab-D, OpenDSS, and MATLAB/Simulink. GridLab-D is typically used for QSTS simulations, but also includes a option to run part of a simulation with a faster timestep in *deltamode*. MATLAB's ODE45 function can be used to solve DAE equations. Simulink's Simscape component blocks can be used to setup QSTS or dynamic simulations. Finally, Opal-RT's power flow solver ePHASORSIM has a simulink interface for running QSTS simulations as well as quasi-steady state dynamical systems.

Chapter 3

Designing PBC feedback controllers

This chapter is based on the paper "Local Phasor-Based Control of DER Inverters for Voltage Regulation on Distribution Feeders" [39], written in collaboration with Elizabeth Ratnam, T.G. Roberts, and Alexandra von Meier.

3.1 Abstract

Phasor-Based Control (PBC) is new control paradigm termed to coordinate Distributed Energy Resources (DER) for improved voltage regulation and other objectives. It comprises a multi-layer control framework where the state of the distribution grid is represented by voltage phasors, and Phasor Measurement Units (PMUs) measure the state at critical points in the distribution grid. In the PBC paradigm, a supervisory controller (S-PBC) sets phasor targets which feedback controllers track. In this paper, we propose a Proportional Integral (PI) implementation for the local control layer (L-PBC), to regulate real and reactive power output of distributed inverters to track a voltage phasor target computed by the supervisory layer. We tune the PI controller gains offline with a genetic algorithm that yields better performance than the Ziegler–Nichols method. We benchmark the proposed L-PBC controller against droop volt-var control (DVVC) and observe improved voltage regulation in simulation on the IEEE 13 node unbalanced test feeder (IEEE 13NF). By means of numerical simulation we observe the response of the L-PBC controllers to small and large grid disturbances. Simulations on larger feeders, IEEE 123-node and 344-node, demonstrate challenges with tuning controllers in setups with different amounts of power-voltage coupling.

3.2 Introduction

The recent rapid growth of distributed energy resources (DER) has spurred increased interest in the opportunity to aggregate DER for participation in ancillary grid services and virtual power plants. However, without careful consideration of the distribution grid physical constraints, there is potential to exacerbate power quality issues related to power flows and voltage variations on the distribution grid.

The increased variability in power output from solar PV, for example, has caused voltage spikes, thermal overloads, and reverse power flow [6]. Legacy voltage regulation equipment such as capacitor banks and load tap changing transformers are limited in their ability to address the issues. Droop Volt-VAR Control (DVVC) of inverters is a popular local control framework among utilities and is adopted by the IEEE1547 integration standard [13]. DVVC is simple to implement, but ensuring good performance can be difficult. The droop curve provides only one controller degree of freedom, motivating the need to modify the slope parameter as grid conditions change [34]. Furthermore, simulations of groups of DVVC inverters indicate a risk of oscillations [40]. Two recent advancements, namely, deployment of μPMUs for measuring a full voltage phasor, and interconnection standards also requiring real power control [13], unlock the potential for better voltage control performance along with other objectives that are critical for distribution grids with high penetration of renewables.

A key limitation of DVVC approach is the inherent steady-state tracking error that potentially causes voltage violations [34]. In [12, 41], an integrator is incorporated into the local controller to eliminate the steady state error in the objective function, but the proposed objective function does not have terms for tracking a voltage phasor, which is core to the PBC paradigm.

To eliminate steady state error when tracking voltage phasors, we consider Proportional Integral Derivative (PID) control. A simple approach for tuning PID control parameters has been proposed by Ziegler–Nichols [42], where the system is brought to the point of marginal stability to determine the critical gain and period, thereby providing some information about the system dynamics. A key limitation of the Ziegler–Nichols method is that it was designed for single-input-single-output (SISO) systems.

Extensions to the Ziegler-Nichols method that have been proposed in the literature focus on applications to MIMO systems. For example, an iterative detuning method is proposed in [43], and a sequential loop closing method is proposed in [44]. However, the former yields conservative tuning parameters resulting in limited performance improvements, and both methods fail to explicitly consider the process interactions that are inherent in MIMO control systems.

In power systems it is conventional to regulate voltage with a SISO controller, where reactive power is controlled to regulate voltage magnitude. That is, reactive power control is decoupled from real power control, where real power is controlled to regulate the phase angle in the grid. While this decoupling approximation is standard in transmission systems, the validity of the method is underpinned by an assumption that line reactance dominates, and resistance (X≫R) can be ignored. Consequently, such a decoupling is less suitable for distribution networks where the resistance of the networks is considered more significant [19].

In accordance with real power affects on voltage magnitude on distribution grids, the IEEE1547 standard (2018 revision) requires inverters to have capability for actuating real power to regulate voltage magnitudes in areas with high DER penetration [13, sec 5.4]. Authors in [45] employ this inverter capability by proposing a switched control method in which reactive power is used until the DVVC controller saturates, at which point real power is used. However, such an approach is conservative since it gives priority to reactive power actuation. In what follows we propose both real and reactive quasi-steady state power control of distributed energy resources (DER) to regulate voltage magnitude and voltage phase angles.

In this paper, we are motivated to find an automated way of PID controller tuning that explicitly considers quasi-steady state power-voltage cross interactions. The main contributions of this work are:

- a novel phasor-based PI-controller for distribution circuits that we benchmark against DVVC,
- an approach for automatic offline calculations of controller parameters considering closed loop system performance, and
- a case study involving a variety of disturbances, the placement of multiple controllers, and the closed loop performance on distribution feeders of different sizes.

3.3 Problem formulation

Phasor-based control employs a multi-layer control hierarchy that decouples high level long-term optimal objectives from short-term power quality objectives [20]. The supervisory layer solves an optimal power flow problem with objectives that can be specified by a utility or other external operator. Some objectives can be very effectively expressed in terms of target voltage phasors at specific nodes, including reducing voltage volatility, balancing three phases, preventing reverse power flow on distribution circuits, and matching voltage phasors across an open switch for topology changes (such as flexible restoration or microgrid islanding). The L-PBC layer is comprised of feedback controllers that send power setpoint commands to one or more dispatchable resources, which are ideally four-quadrant controllable DER/inverter combinations. The S-PBC uses an Optimal Power Flow (OPF) solution to periodically send phasor targets to the L-PBC. These targets are defined relative to the voltage at a reference node (e.g. the substation), and directly enforce operating voltage limits (e.g. ±5% of nominal). The use of the phasor as a network state variable enables an immediate corrective response to disturbances without communication among L-PBCs and without compromising privacy.

In the context of PBC, we design the L-PBC layer in which inverter real and reactive power is actuated to regulate voltage magnitude and voltage phase angle, which is consistent with the approach proposed in [46]. Specifically, real and reactive power commands are sent to inverter resources at "actuator nodes" to drive the voltage phasor at the "performance node" to the S-PBC computed target phasor. Leveraging the structure of a Proportional Integral (PI) controller we overcome limitations of a single control degree of freedom (e.g., Proportional (P) control) for improved steady-state tracking. For each phase and node with an inverter, two PI controllers with the structure

$$Q_{cmd}[k+1] = m_p^q(V[k] - V_{target}[k]) + m_i^q \sum_1^k (V[k] - V_{target}[k]) \text{ for } k = 1...n \tag{3.1}$$

$$P_{cmd}[k+1] = m_p^p(\delta[k] - \delta_{target}[k]) + m_i^p \sum_1^k (\delta[k] - \delta_{target}[k]) \text{ for } k = 1...n \tag{3.2}$$

are implemented to compute inverter commands. At time $k\Delta$ (where Δ is the time interval between time step k), the voltage magnitude is denoted by $V[k]$, the voltage phase angle is denoted by $\delta[k]$, the real power command is denoted by $P_{cmd}[k]$ and the reactive power command is denoted by $Q_{cmd}[k]$. Further, m_p^q, m_i^q, are the design parameters for our controller C_1, and m_p^p and m_i^p are the design parameters for our controller C_2. The phasor target values $V_{target}[k]$ and $\delta_{target}[k]$, are specified by the S-PBC.

Feedback controller design

In this section we describe a two-part process to design the controller parameters m_p^q, m_i^q,m_p^p and m_i^p. First, we describe an online measurement process to determine power-voltage sensitivities. Then we incorporate the sensitivities into a closed-loop model of the PBC system that can be evaluated with an offline tuning algorithm.

While the algebraic power flow equations relating nodal power injections to voltages express $P = f_1(V, \delta)$ and $Q = f_2(V, \delta)$, the inverse mapping, $V = g_1(Q, P)$ and $\delta = g_2(Q, P)$, is difficult to express without an accurate estimate of the grid's effective impedance. In what follows we use a power flow simulator from Opal-RT, ePHASORSIM, to characterize this inverse relationship for various feeders. Specifically, we seek the sensitivity map H introduced in section 2.1 that describes how the change in steady-state nodal power on each phase of the actuation node impacts the change in steady-state voltage on each phase of the performance node. We define H by

$$H = \begin{bmatrix} H_{vq} & H_{vp} \\ H_{dq} & H_{dp} \end{bmatrix}, \tag{3.3}$$

and each element in H is defined as

$$H_{vq} = \max_{i \in \{1,...,M\}} a_i = \max_{i \in \{1,...,M\}} \left(\frac{V_i^{ss} - V^0}{Q_i^{ss} - Q^0} \right),$$

$$H_{vp} = \max_{i \in \{1,...,M\}} b_i = \max_{i \in \{1,...,M\}} \left(\frac{V_i^{ss} - V^0}{P_i^{ss} - P^0}, \right),$$

$$H_{dq} = \max_{i\in\{1,\ldots,M\}} c_i = \max_{i\in\{1,\ldots,M\}} \left(\frac{\delta_i^{ss} - \delta^0}{Q_i^{ss} - Q^0}, \right),$$

$$H_{dp} = \max_{i\in\{1,\ldots,M\}} d_i = \max_{i\in\{1,\ldots,M\}} \left(\frac{\delta_i^{ss} - \delta^0}{P_i^{ss} - P^0}, \right),$$

where index i corresponds to each of M step changes applied to the initial reactive power Q^0 (or real power P^0), where the initial operating point is (Q^0, V^0) (or (P^0, δ^0)).

In more detail, to compute H_{vq} we measure the initial reactive power Q^0 and voltage magnitude V^0 at the respective operating point (Q^0, V^0). Then, we apply a step change in reactive power and measure the steady-state reactive power Q_1^{ss} and the steady-state voltage magnitude V_1^{ss}, corresponding to operating point (Q_1^{ss}, V_1^{ss}). We denote by V_i^{ss} the measured steady-state voltage magnitude after each step change i. In this way we compute $\alpha = \{a_1, \ldots, a_i, \ldots, a_M\}$, where a_i corresponds to step change i. The maximum element in α is assigned to H_{vq}.

By way of an example, in Fig. 3.1 we consider the IEEE 13-node feeder [3] where the actuator and performance node are co-located at node 675. Our initial operating point is given by $(Q^0, V^0) = [0\text{pu}, 1\text{pu}]$, and we consider $M = 10$ step changes in the reactive power output. We compute α for step changes $Q_i^{ss} = \{20, 50, 70, 100, 150, 300, 500, 750, 1000\}$ (in kVARs). The maximum of α, that is, $a_1 = 0.095$ is assigned to H_{vq}, an element in H. Note that changing the location of the actuator node or the performance node would result in different gains a_i.

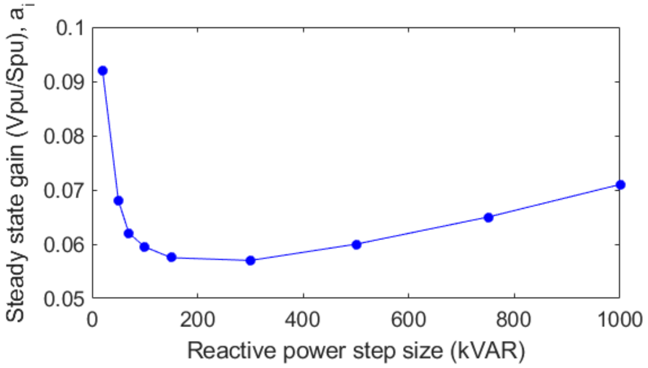

Figure 3.1: steady-state gains a_i for different step inputs on the IEEE 13NF, where operating point before each step change is $(Q^0, V^0) = [0\text{pu}, 1\text{pu}]$. Note that $H_{vq} = \max_{i\in\{1,\ldots,M\}}$, where i is the step change index.

In Fig. 3.2 we represent our control system in block diagram form. Each controller C_1, C_2, is a discrete time PI controller, defined by the control law in (3.1) and (3.2). The output of the H mapping is added to the measured voltage phasor. We seek to drive the measured voltage phasor (V, δ) to the specified target values (V_{target}, δ_{target}). The two controllers are decoupled, but each is tuned to consider the cross interactions of the process when both loops

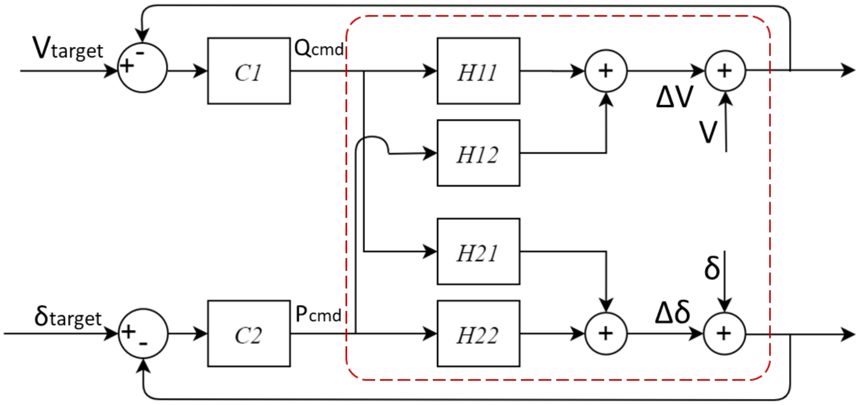

Figure 3.2: Block diagram representation of our control system, with controllers C_1 and C_2 and gains $H_{11}, H_{12}, H_{21}, H_{22}$ [2].

are operating simultaneously. These cross interactions are significant due to non-negligible distribution circuit resistance.

Tuning with Genetic Algorithm

Next, for each of controller C_1, C_2, we sample sets of candidate controller parameters from a heuristically-defined parameter space. Specifically, we sample $m_p^q, m_i^q \in (0, \frac{0.7}{H^{vq}})$ and $m_p^p, m_i^p \in (0, \frac{0.7}{H^{dp}})$. For each candidate set of four parameters, we evaluate the performance of the closed loop, quasi-steady state, step response of the system in Fig. 3.2. The parameter set that minimizes a genetic algorithm cost function J is assigned to C_1 and C_2.

The genetic algorithm cost function enforces weighted tradeoffs between four terms as shown in equation (3.4). The terms penalize quasi-steady state tracking error $|y_{ref} - y_k|$, control effort u_k, quasi-steady state settling time v, and quasi-steady state overshoot w, respectively. The first two terms are discrete accumulators over the evaluation horizon N, and the last two terms each enforce a hard constraint on the controller designs according to a specified maximum quasi-steady state settling time or overshoot. Both $\eta(v)$ and $\zeta(w)$ are log barrier functions [47] which are assigned a quadratically increasing penalty that sharply rises when a quasi-steady state settling time or overshoot violation occurs.

$$J = \sum_{k=1}^{N} Q|y_{ref} - y_k| + \sum_{k=1}^{N} R|u_k| + v\eta(v) + w\zeta(w) \tag{3.4}$$

In cases where we have more than one actuator connected to the same phase, the control parameters computed with the genetic algorithm are divided by the number of actuators connected to the respective phase. That is, if there are three single-phase actuators on phase A at different nodes, the controller parameters associated with those actuators are divided by three to obtain m_p^q, m_i^q, m_p^p, and m_i^p. This division operation considers the interaction between actuators on the same phase.

3.4 Numerical Simulations

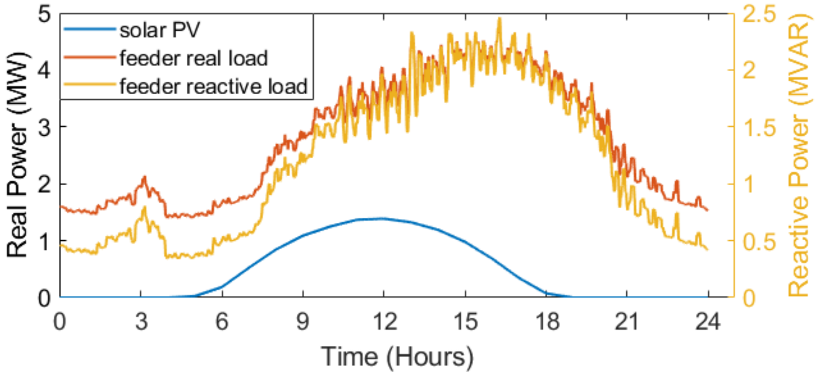

Figure 3.3: Total generation and load on the IEEE 13NF across 24 hours.

In the simulations that follow, reported spot loads on IEEE feeders or otherwise are replaced with aggregate second-wise time-varying net load data. The data is generated based on public commercial and residential loads and solar PV generation profiles from Southern California Edison during a typical summer day. We consider a PV penetration level at 50% of the non-coincident feeder peak. Fig. 3.3 shows the real and reactive power generation and load across the day for the 13NF.

We consider an L-PBC implementation of controllers C_1 and C_2 to coordinate multiple actuators on phase A, B, and C at different nodes. Specifically, on the IEEE 13NF we place the performance node at 632 and the actuator nodes at 634, 675, and 645, as illustrated in Fig. 3.4. It is worth mentioning that the actuator at node 645 is on a single phase B. In total, there are two actuators on phase A tracking the voltage phasor at node 632a, three actuators phase B tracking the phasor at 632b, and three actuators on phase C tracking the phasor at 632c. We compare the genetic algorithm method of tuning the PI design parameters for C_1 and C_2 to the Ziegler–Nichols method.

With the Ziegler–Nichols tuning method, the gains of each controller C_1, C_2 are found for each phase, one at a time leveraging the Opal-RT ePHASORSIM simulator. We observe that when both controllers C_1 and C_2 are operating in closed loop, the quasi-steady-state voltage output grows indicating voltage instability. Consequently, via trial and error, we detune the respective gains by 30% to enable steady-state tracking.

Next, we use the proposed genetic algorithm to find the design parameters for C_1 and C_2. Table 3.1 compares the design parameters for Phase B when implementing (1) the proposed genetic algorithm, and (2) the detuned Ziegler-Nichols method.

		Ziegler–Nichols	Genetic Algorithm
675a to 632a	m_p^q	1.16	1.39
	m_i^q	0.63	1.54
	m_p^p	0.02	0.0044
	m_i^p	0.013	0.032
634a to 632a	m_p^q	1.13	0.69
	m_i^q	0.62	1.62
	m_p^p	0.028	0.0042
	m_i^p	0.017	0.030
675b to 632b	m_p^q	1.16	0.593
	m_i^q	0.63	1.62
	m_p^p	0.02	0.0068
	m_i^p	0.013	0.0317
634b to 632b	m_p^q	1.13	0.123
	m_i^q	0.62	1.65
	m_p^p	0.028	0.0023
	m_i^p	0.017	0.033
645b to 632b	m_p^q	1.98	1.69
	m_i^q	1.08	1.91
	m_p^p	0.078	0.013
	m_i^p	0.047	0.0287
675c to 632c	m_p^q	1.16	0.88
	m_i^q	0.63	1.82
	m_p^p	0.02	0.0067
	m_i^p	0.013	0.0278
634c to 632c	m_p^q	1.13	1.47
	m_i^q	0.62	1.71
	m_p^p	0.028	0.013
	m_i^p	0.017	0.035

Table 3.1: C_1 and C_2 controller parameters for the for the simulation involving multiple actuators. Control parameters $m_p^q, m_i^q, m_p^p, m_i^p$ are in kVAR/V, kW/V, kVAR/degrees, and kW/degrees respectively

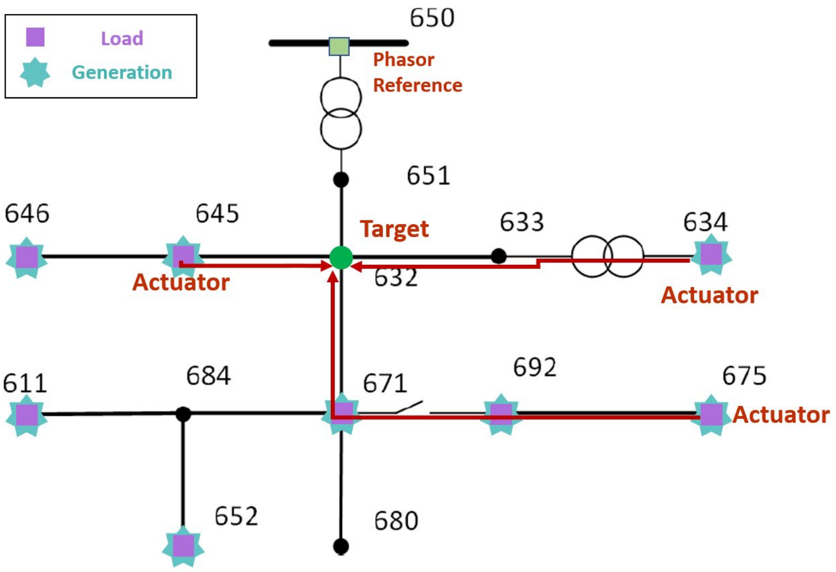

Figure 3.4: Diagram of the IEEE 13NF with labels included for the phasor target node and actuator nodes, as considered in the multiple actuator simulation.

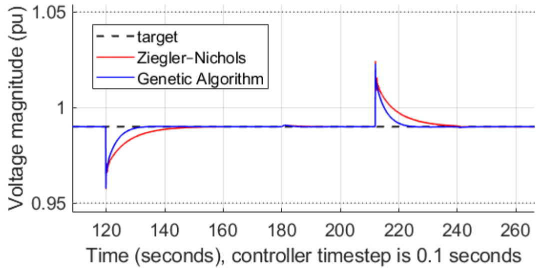

(a) Comparison of the quasi-steady state voltage magnitude response to a square wave disturbance for the IEEE 13NF, node 632a, where controllers C_1 and C_2 on each actuator node are tuned with parameters in Table 3.1.

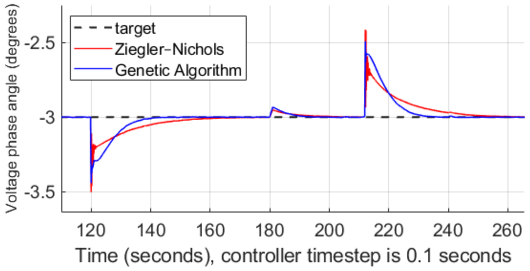

(b) Comparison of the quasi-steady state voltage angle response to a square wave disturbance for the IEEE 13NF, node 632a, where controllers C_1 and C_2 on each actuator node are tuned with parameters in Table 3.1.

In Fig. 3.5a and Fig. 3.5b we consider tuning the L-PBC design parameters in two ways, (1) Ziegler-Nichols then detuning by 30%, and (2) the proposed genetic algorithm. We consider the closed loop voltage magnitude and phase angle response at node 632a, when applying a square wave disturbances at nodes 634a/b/c, 671a/c, 675a/b/c, 692/c, and 611/c. We observe that the L-PBC controller tuned via the proposed genetic algorithm allows for a faster steady-state convergence to the target phasor.

Six-hour Simulation

Here we compare PBC to DVVC on the IEEE 13NF from 9:00 to 15:00. While DVVC is designed to regulate local voltages, the tracking of phasor targets by L-PBCs contributes to meeting S-PBC higher level objectives across potentially multiple feeders. In addition to the global objectives achieved, we show that the voltage magnitude regulation compared to DVVC is improved.

For the purposes of comparison, in this simulation the supervisory layer sends minute-wise phasor targets to nodes 634, 671, 675, and 632, which have co-located L-PBCs. As such, we have multiple performance nodes with co-located controllers and actuators. For the DVVC case, we place controllers at the same four three-phase nodes. The twelve controllers actuate 600kVA inverters, where the objective is to track the phasor target at the respective nodes.

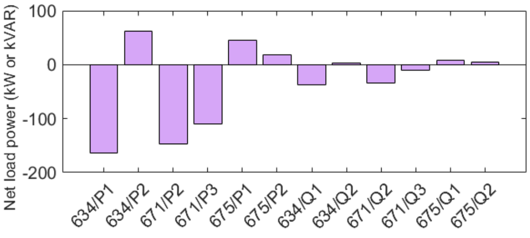

(a) Load disturbance at 11:07 from the six-hour simulation.

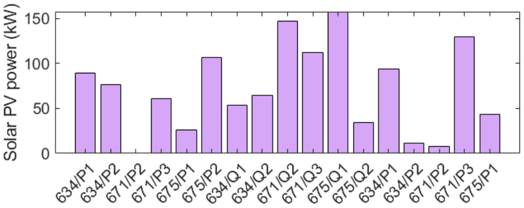

(b) Cloud cover event at 12:17 from the six-hour simulation.

Large signal disturbances can be caused by several physical events, such groups of people changing their loads at once, clouds briefly covering solar panels, and switching events. These disturbances can be modeled with either a step or square wave disturbance in net load. To capture a variety of large-signal disturbances, every fifteen minutes real power disturbances are randomly sampled from 40 to 800 kW and duration ranges are sampled from 10s to 350s. Reactive power disturbances are sampled from 0.9 leading to 0.9 lagging to represent a variety of inductive and capacitive loads.

For controller parameters, the DVVC slope is usually calculated from the inverter's maximum available reactive power and the allowable voltage range [13]. However, tuning the twelve controllers in that way causes voltage instability for this setup. Instead the DVVC slopes are computed using the genetic algorithm. For fair comparison, the DVVC nominal voltage is set equal to the time-varying PBC voltage magnitude target.

We next consider two scenarios to simulate PBC. First, PBC regulates both voltage magnitude and angle (Scenario 1). Second, PBC regulates voltage magnitude using reactive power alone - which is more similar to DVVC (Scenario 2). In Fig. 3.7 we observe the voltage magnitude at node 634b with no control, DVVC, PBC without real power regulation, and PBC with both real and reactive power regulation. Controllers operating with DVVC are unable to keep the voltage within the 5% range in the middle of the day. PBC controllers in Scenario 2 eliminate the steady-state error and 5% violations. However, in Fig. 3.8 we observe more apparent power ($S = \sqrt{P^2 + Q^2}$) actuation with PBC under Scenario 1 than with DVVC. In contrast, PBC under Scenario 1 improves the voltage regulation while also enabling supervisory level objectives to be achieved.

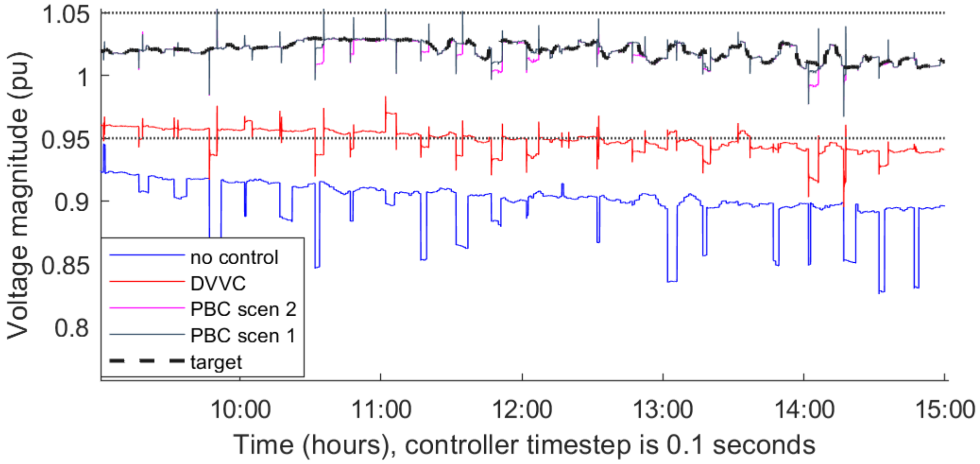

Figure 3.7: Voltage magnitude at node 634a of the IEEE 13NF for different control laws: (1) no control, (2) droop volt-var control (DVVC), (3) PBC Scenario 2, (4) PBC Scenario 1.

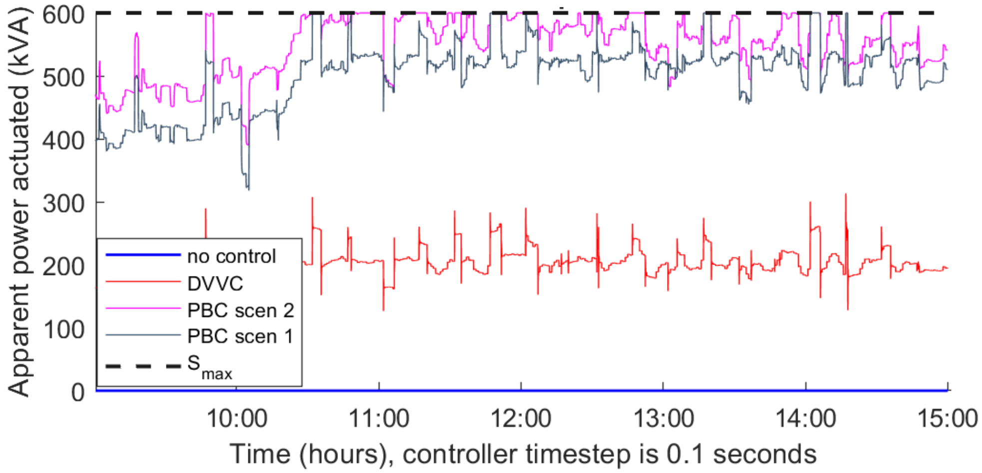

Figure 3.8: Apparent power actuation at node 634a of the IEEE 13NF for different control laws: (1) no control, (2) droop volt-var control (DVVC), (3) PBC Scenario 2, (4) PBC Scenario 1.

Metrics are computed for individual phases across the simulation duration, then the best, average, and worst case of each metric across all nodes of the IEEE 13NF are computed.

The average quasi-steady state tracking error γ is computed by

$$\gamma = \frac{\sum_{n=1}^{N}(\frac{|V-V_{target}|}{V_{target}} \times 100)}{N}. \tag{3.5}$$

The voltage volatility index (VVI) is computed based on ANSI standards [10], in which a violation is counted if the voltage at the node violates either 1) 1.06-0.9pu band instantaneously (range A) or 2) 1.05-0.95 pu band continuously for 2 minutes (range B). Finally, apparent power actuation ($S = \sqrt{P^2 + Q^2}$) averaged over time is compared, as well as the percent of time the actuators are saturated due to the large signal disturbances.

Metrics	Worst		Best		Average of all phases	
	DVVC	PBC scen. 1	DVVC	PBC scen. 1	DVVC	PBC scen. 1
Average tracking error (%)	7.040	0.059	0.305	0.016	2.660	0.075
Percent of 5% sustained violations (%)	31	0	0	0	0	0
Number of instantaneous violations	3	16	1	0	1.2	1.5
Average actuation (kVA)	220.17	600.00	1.15	211.01	65.53	359.25
percent saturated (%)	0	34.82	0	0	0	6.03
Average quasi-steady state overshoot (%)	–	21.16	–	4.61	–	10.80
Average quasi-steady state settling time (seconds)	–	3.80	–	1.45	–	2.33

Table 3.2: Comparison of performance metrics for DVVC and PBC among the twelve controlled phases (four nodes with three phases) across the six-hour simulation. Best and worst values are not coincident.

In Table 3.2 we present the computed metrics for the control laws DVVC and PBC Scenario 1 from the six-hour simulation. The quasi-steady state average tracking error is significantly reduced with PBC Scenario 1 and 2 due to the integrator action eliminating steady-state error. Furthermore, for Scenario 1 and 2 we observe no load change disturbances that result in sustained violations (range B), while with DVVC 31% of the 2-minute disturbances persist outside the 5% range. In this undervoltage scenario, PBC raises the voltage magnitude to track the phasor target, resulting in sustained voltages above 1.06 Vpu for a short period of time. DVVC requests less total inverter actuation, but does so at the expense of voltage regulation performance.

	IEEE 13NF	IEEE 123NF	344NF
Node number	675c	76c	300063911c
H_{vq}	0.27	0.17	−0.048
H_{vp}	0.14	0.098	0.066
H_{dp}	14.4	10.66	11.94
H_{dq}	−5.51	−4.52	−4.85
m_p^q	0.97	0.180	3
m_i^q	1.81	0.772	0.5
m_p^p	0.011	0.011	0.048
m_i^p	0.023	0.013	0.028

Table 3.3: PBC design variables obtained using the genetic algorithm, where the controller parameters and H gains are provided for phase C of the co-located actuator and performance node on each of the unbalanced feeders IEEE 13NF, IEEE 123NF, and 344NF.

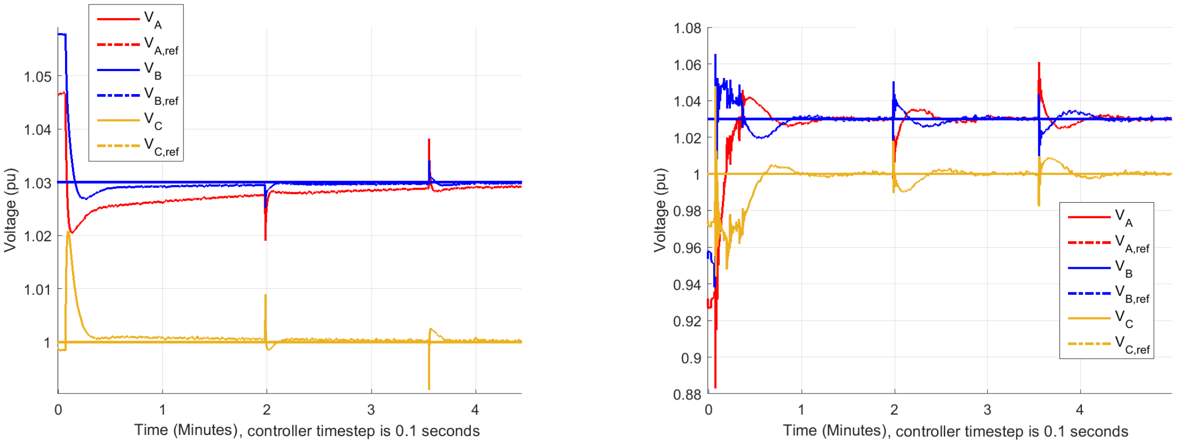

(a) Quasi-steady state voltage magnitude response to a square wave disturbance where actuator and performance node are at node 76 of the 123NF.

(b) Quasi-steady state voltage phase angle response to a square wave disturbance where actuator and performance node are at node 300063911 of the 344NF

Scaling Simulation

A co-located performance and actuator node are placed on three-phases far from the feeder head, namely node 675 for the IEEE 13-node feeder (13NF), node 76 for the IEEE 123-node feeder (123NF), and node 300062503 for a 344-node [1] feeder from PG&E (344NF). A square-wave disturbance of 300kW and 59kVAR is applied to the performance node on each feeder, and actuator limits are turned off. The grid steady-state gains H_{vp},H_{vq},H_{dq}, and H_{dp}

---

[1] in original publication [39] was erroneously referred to as having 647 nodes

recorded in Table 3.3 provide insight into the difficulty of finding parameters for controllers C1 and C2 on each phase.

Consider the ratio of coupling to decoupling steady-state gains $r_1 \triangleq \frac{H_{vp}}{H_{vq}}$ and $r_2 \triangleq \frac{H_{dq}}{H_{dp}}$. Loop coupling is significant if r_1 or r_2 are large in magnitude, and if the sign is negative the loops adversely affect each other. The IEEE 13NF has minimal coupling for both control loops, while 123NF and 344NF has significant coupling for controlling voltage magnitude (r_1). Coupling directly causes adverse interactions between the C_1 and C_2 controllers, resulting in actuator saturation or voltage instability. While detuning can improve steady-state tracking in some cases, we find it does not for the setups that have significant coupling.

The genetic algorithm is successful in tuning controllers for the IEEE 13NF and IEEE 123NF, but the significant coupling in the 344NF causes the method to fail. Controller parameters for that feeder are found through developed intuition. Parameters for phase C are collected in Table 3.3.

The voltage magnitude for the simulation of the IEEE 123NF and 344NF are shown in Fig. 3.9a. The phase angle is omitted, but behavior on both feeders is similar to that of 3.5a(b). The IEEE 123NF has long voltage magnitude settling time due to significant coupling on the feeder [2]. We observe more volatility in voltage magnitude and phase angle on the largest feeder, the 344NF, potentially because there are more nodes with time-varying load and generation.

3.5 Conclusion

We have presented an implementation of the local layer of Phasor-Based Control (PBC), in which inverter-based resources are sent real and reactive power commands so that voltage phasors at specified nodes reach target phasors. Commands are computed with PI controllers that explicitly considers the distribution grid impedance coupling. The controllers are tuned using a steady-state gain relationship between power and voltage, and a genetic algorithm that identifies controller gain based on a quasi-steady state closed loop grid model. Numerical simulations on the IEEE 13NF show tuning with the proposed genetic algorithm method yields better tracking performance than the Ziegler–Nichols method. By comparing DVVC with two scenarios of PBC, we observe improved voltage regulation for both PBC scenarios. Coupling between the voltage magnitude and phase angle on the 344NF is found to cause adverse interactions between the controllers, causing the PBC tuning method to fail. Better characterizing this coupling interaction will be investigated in the future.

---

[2] When parsing the public 123NF data, all line self impedances z_{22} and mutual impedances z_{31} were erroneously swapped, resulting in tests that are done on a feeder with unrealistically high mutual impedances. The 123NF was corrected for use in Chapter 5

Chapter 4

Hardware-in-the-Loop Testing

This chapter is based on the (in preparation) paper "Hardware in the Loop Benchmarking for Phasor-Based Control Validation" [48], written in collaboration with Maxime Baudette, Leo Chu, Christoph Gehbauer, Keith Moffat, Jasper Pakshong, and Alexandra von Meier.

In this section we describe the hardware implementation PBC, which includes both the S-PBC and L-PBC hierarchical layers. In particular, we are validating the L-PBC PI control law and tuning algorithm presented in Chapter 3. Hardware-in-the-loop (HIL) experiments were performed at the Lawrence Berkeley National Lab microgrid testing facility called FLEXLAB.

4.1 Flexgrid Test Bed

A schematic of the experimental setup is shown in Fig. 4.1. The facility's microgrid has a single three-phase bus to which a Photovoltaic (PV) / battery system is connected. The system comprises three 8.3 kVA SolarEdge smart inverters that each interface a Tesla Powerwall 3.3 kw / 6.4 kWh battery and 3.75 kW PV strings. Because the full PV installation amounts to 15 kW, one of the inverters is connected to two PV strings. The micro-grid is equipped with a micro Phasor Measurement Unit (μPMU)[1] that measures the three-phase voltages and currents at its point of connection. The local grid connection can be swapped to a three-phase 30 kVA grid emulator that is interfaced with an Opal-RT real-time digital grid simulator.

The control loop is comprised of μPMU measurements being sent to a controller to compute power commands for inverter and load rack actuators. For the default mode of the facility's inverter control, an *integer* percentage value of the active power limit and a *real* power factor value are provided as commands. Because this mode was not providing sufficient precision, we setup an advanced control mode that specifies active and reactive power commands as a *real* percentage value, allowing us to emulate four-quadrant operation

---

[1] μPMU commonly refer to a PMU for the distribution grid

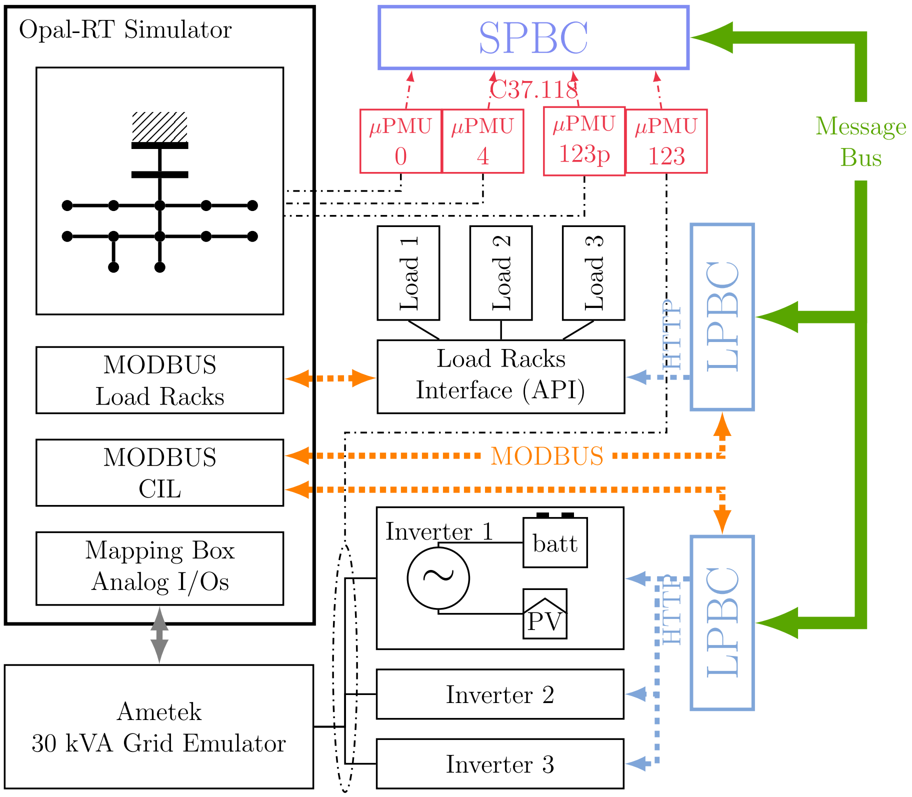

Figure 4.1: Schematic of the experimental setup at FLEXLAB

of the inverters. A set of custom load racks built with a set of fans and their respective variable-frequency drive (VFD) totalling to 1000 W were also sent real power commands. Because the reactive power consumption of the load racks was an uncontrolled variable, these values were zeroed out before being fed to the grid simulation.

Real-time simulation

The grid simulation is performed in real-time with Opal RT's power flow simulator ePHASORSIM, which is has an interface based on Simulink. The test setup enables Power Hardware-in-the-Loop (P-HIL) experiments, where the grid emulator is mapped to a chosen bus in the simulation. The reference node is located at the substation for all tests and is primarily used as common reference to compute the angles of the other phasor measurements. The three-phase PV and battery system was originally connected in a Delta configuration to a step up 208/240 transformer that allows it to run at a 240 V voltage level using the local three-phase 120 V distribution grid (208 V in line-to-line voltage). For the PBC tests, a set of three-way switches was added to allow the connection of the micro-grid in a Wye configuration. This allowed three seperate actuators to be mapped to different nodes in the grid simulator. See [48] for details on the HIL setup.

Communication setup

The smart inverters allow for remote control of the PV and battery system over the MODBUS communication protocol. The S-PBC and L-PBC PI control was implemented in Python and commands are communicated to the actuators via a publish-subscribe message bus the Distributed, Extensible, Grid Control (DEGC) platform. The S-PBC provided new phasor targets every minute, while the feedback controller operated on a 15-second cadence. The PMUs reported 120 measurements each second. See [49] for details on the communication setup.

Controller-In-the-Loop (CIL)

The basic HIL setup loop involves real-time measurements being fed to a controller, which computes a command that is sent to physical actuator. Then the actuator's action informed the next measurement. In contrast, in a CIL setup, the physical actuator is omitted from the loop, and the actuator's action is exactly determined by the controller command. That is, the controller prototype is integrated with the real-time grid simulator over a digital link using MODBUS over IP. Thus CIL is an intermediate setup between software simulations and HIL testing. A toggle in the model and on the physical controllers allows us to receive CIL or HIL actuator input.

4.2 Experiments and Results

In this section we compare voltage phasor tracking and actuator effort between software, CIL, and HIL tests. We include one test from each of the IEEE 13-node unbalanced (13NFunbal), 13-node balanced (13NFbal), 33-node balanced (33NFbal), and a 344-node unbalanced PG&E distribution feeder (341NFunbal).

For all tests, we included time-varying load data profiles that were constructed as follows. Reported spot loads on IEEE feeders or otherwise were replaced with aggregate second-wise time-varying net load data. The data is generated based on public commercial and residential loads and solar PV generation profiles from Southern California Edison during a typical summer day. We considered a PV penetration level at 100 % of the non-coincident feeder peak. Fig. 4.2 shows the net active and reactive power of uncontrolled PV and loads on each node of the 13NFunbal across a typical day. Observe that the 100 % PV penetration causes some slightly negative net loads during our simulation window of 11am-11:50pm. Actuator limits were set at 500 kW and 500 kVAr for all tests in software, CIL, and HIL.

For all software tests, controllers turned on when the simulation began, at 11:00am. We used a simulation timestep of fifteen seconds, to match the HIL setup's expected delay of fifteen seconds between consecutive control actions. For teh software tests, the Proportional-Integral (PI) controller parameters were designed using the offline genetic algorithm method described in Chapter 3. For CIL and HIL tests the controller gains were modified to improve the controller's response when implemented in hardware.

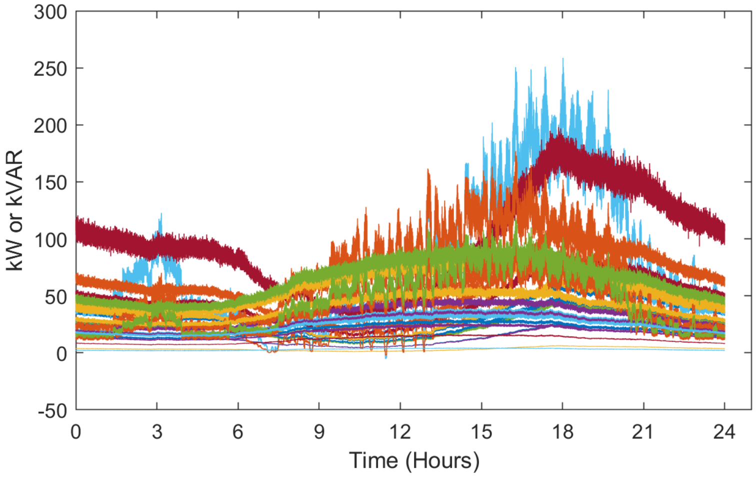

Figure 4.2: Daily active and reactive power net load profiles of the 13NFunbal

33-Node Balanced Grid

On the 33NFbal we placed inverters on three-phases of node 18 and load racks on three-phases of node 26, both to track the 3-phase phasor target at node 6. The phasor target was constant at $0.97Vp.u$ and $-0.5°$ on three phases. In addition to the voltage disturbances caused by the time-varying load and PV data, we applied two sets of square wave disturbances at nodes 6, 13, 21, 25, and 26 from 1080 to 1440 and 2160 to 2520 seconds, equal to 300 % of the nodal active and reactive power.

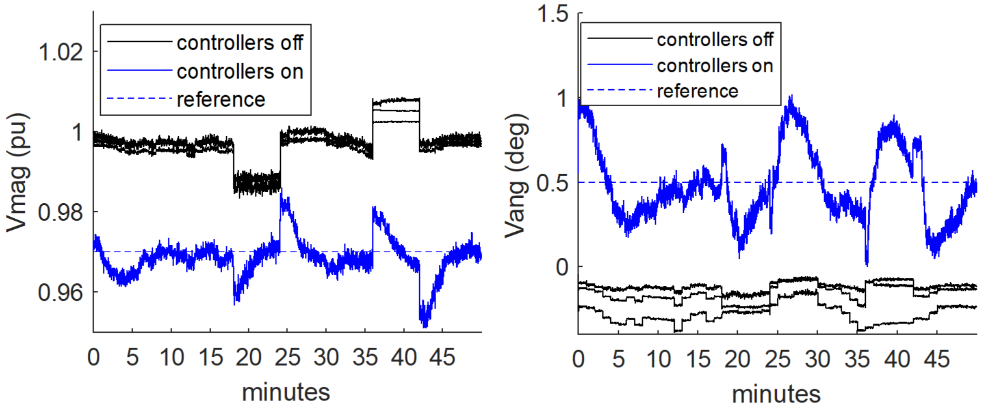

Figure 4.3: Comparison of voltage magnitude and phase angle between software and HIL tests on the 33NFbal

In Fig. 4.3 we compare voltage magnitude and phase angle at the performance node when the controllers are turned off and when they are on. We observe that the curves for each phase are close to overlapping, due to the feeder being balanced. When the controllers are on they successfully drive the target on each phase to its target both when the simulation begins and when rejecting each step of the large load disturbances.

Typically, the communication setup for inverter control is local, where inverters use measurements at their own node to modify their power output with the goal of regulating voltage and/or frequency. Hence it is notable that in this setup we demonstrate three-phase devices actuating at two different nodes to collaboratively track the three-phase voltage magnitude and phase angle target at a third node.

13-Node Unbalanced Grid

On the 13NFunbal we place inverters on three-phases of node 675 and load racks on three-phases of node 671, both to track the phasor target at node 632. The phasor target is constant at 0.99 $Vp.u$ and $-1°$ on three phases. In addition to the voltage disturbances caused by the time-varying load and PV data, we apply two sets of square wave disturbances at nodes 623, 671, 675, 632, and 645 from 1080 to 1440 and 2160 to 2520 seconds, equal to 90% of the nodal real and reactive power.

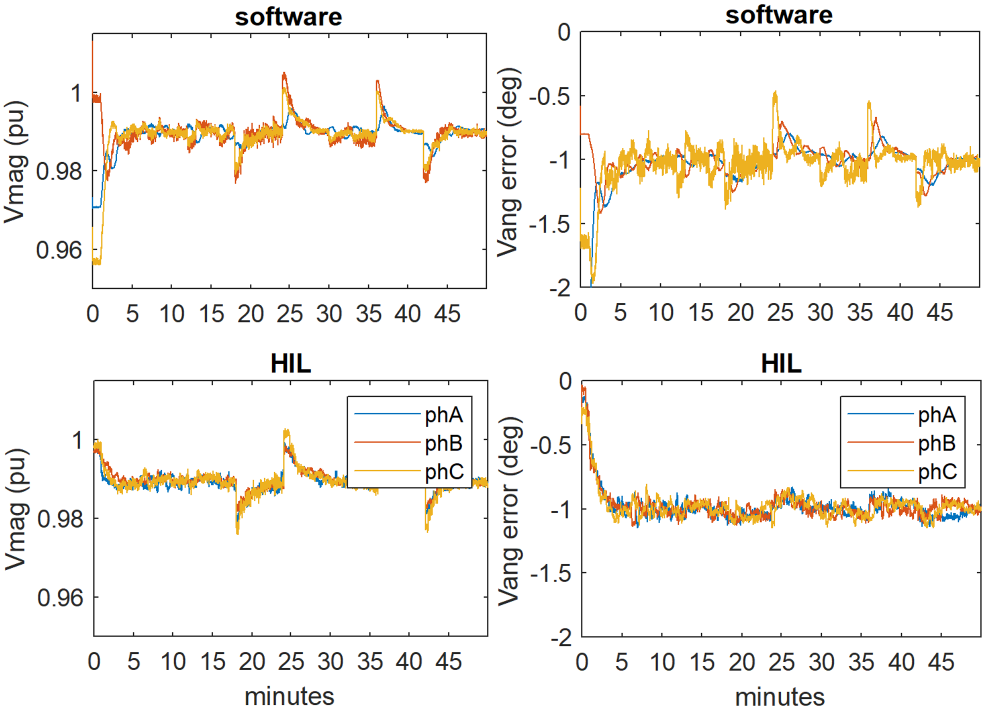

Figure 4.4: Comparison of voltage magnitude and phase angle between no-control, software, and HIL tests on the 13NFunbal

In Fig. 4.4 We compare the performance of the PI controllers between software and HIL tests by plotting the voltage magnitude and phase angle at the performance node. We observe convergence to the phasor target both when the simulation begins and when rejecting each step of the large load disturbances. This test demonstrates that our setup and control algorithm is successful on an unbalanced distribution grid.

13-Node Balanced Grid

On the 13NFbal we place inverters on phase A of node 671, 652, and 692 to track the phase A targets at the same locations (co-located tracking setup). There are no square wave disturbances, but the phasor target is changed twice in real-time to illustrate a scenario in which the L-PBC handles problematic phasor targets.

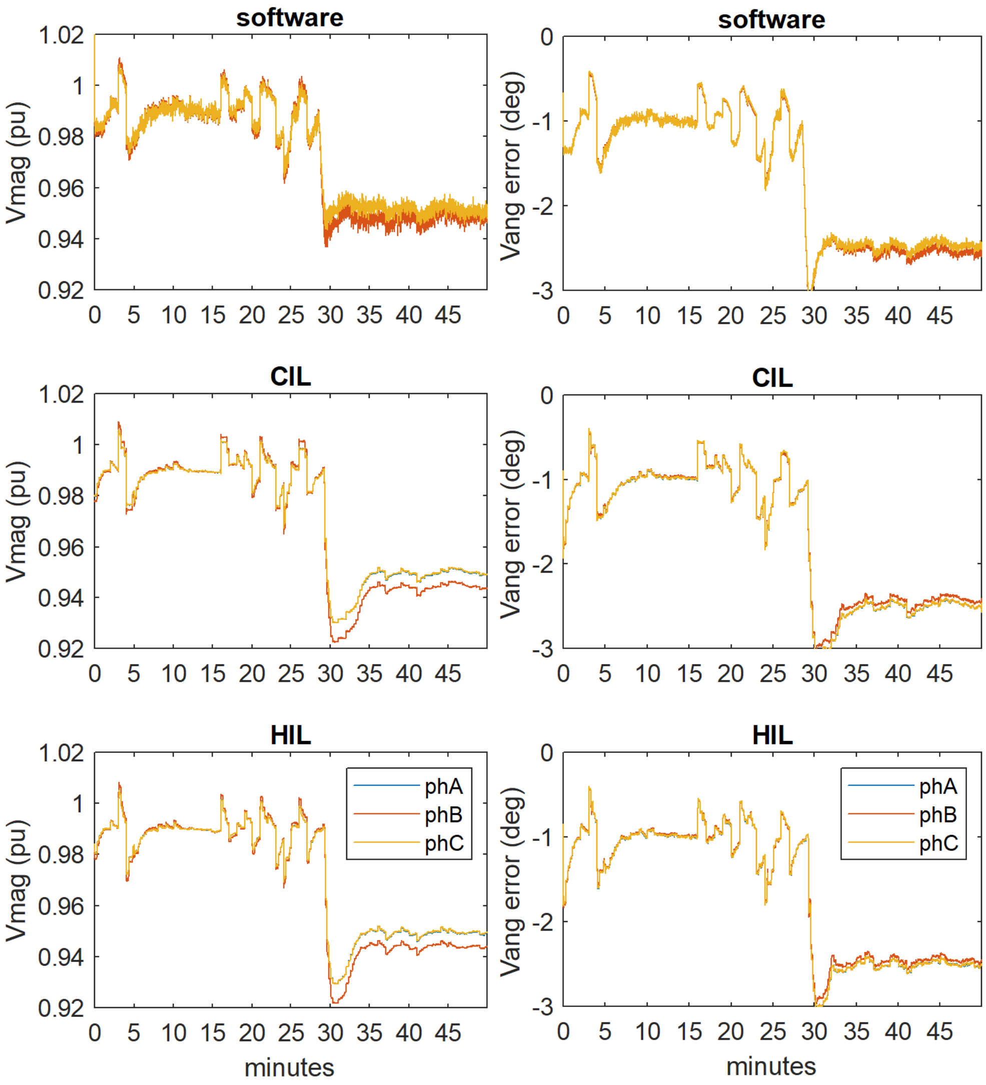

Figure 4.5: Comparison of voltage magnitude and phase angle between software, CIL, and HIL tests on the 13NFbal

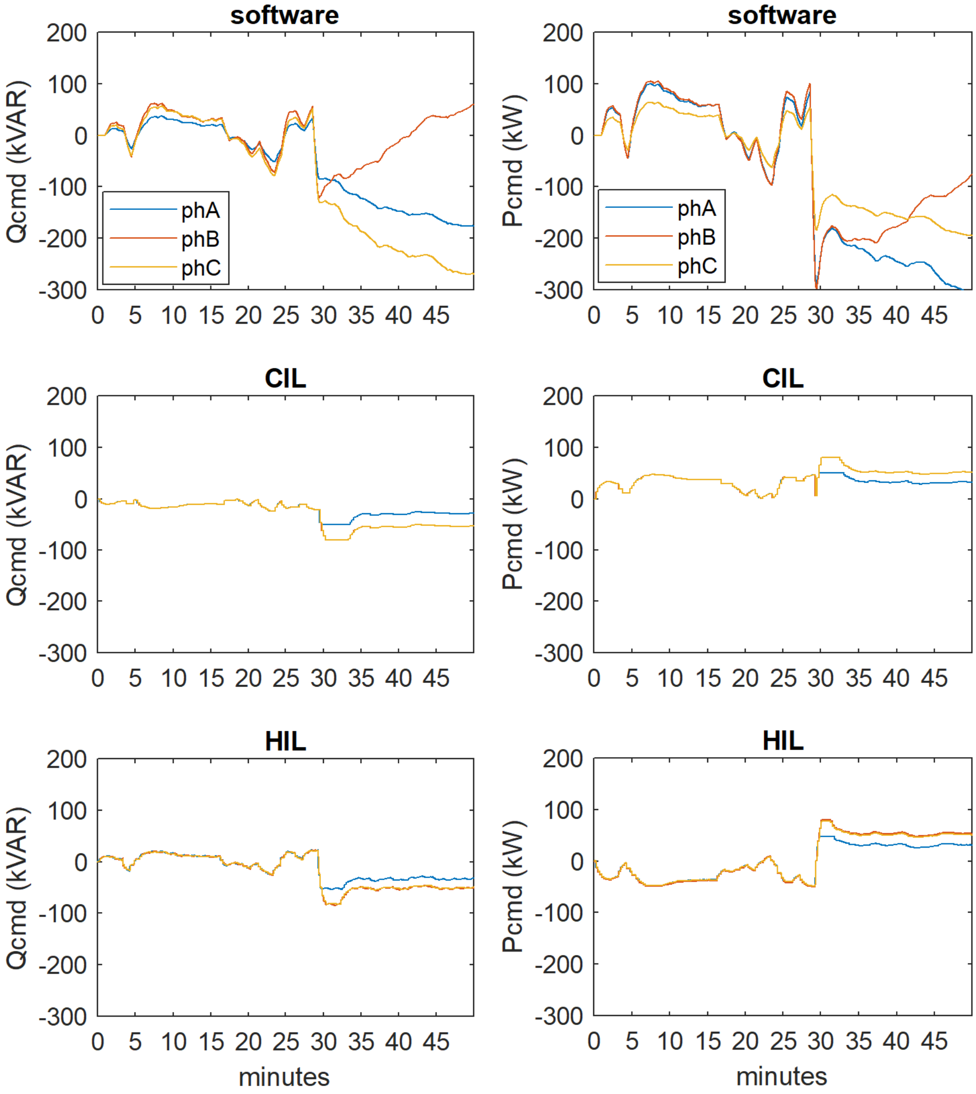

Figure 4.6: Comparison of inverter real and reactive power actuation between software, CIL, and HIL tests on the 13NFbal

The test is conducted in software, CIL, and HIL. We plot the voltage magnitude and phase angles in Fig. 4.5, and in Fig. 4.6 we plot real and reactive power inverter actuation.

The S-PBC initially sent the L-PBC an achievable magnitude and angle target of 0.99 $Vp.u$ and $-1°$ on three phases. After 30 minutes (1750 seconds), the targets were updated to $0.92Vp.u$ and and $-4°$, which were not achievable with the available actuation of 500kW/500kVAR. After reaching saturation, the L-PBC alerts its saturated status to the S-PBC, causing the S-PBC to send back an updated phasor target of $0.95Vp.u$ and $-2.5°$ at 1800 seconds. Finally, the feedback controller at 671 tracked this target with a successful, non-saturated status. This test demonstrates effective communication between the L-PBC and S-PBC during HIL.

PG&E Unbalanced Grid

Finally, to assess the scalability of PBC we conduct tests on the 344NF. We place inverters on three-phases of node 300063911 that track the phasor target at the same node. The phasor target is constant at 0.98 $V p.u$ and $-3°$ on three phases. Time-varying load and PV data causes second-wise disturbances that the controllers must reject to maintain the phasor target.

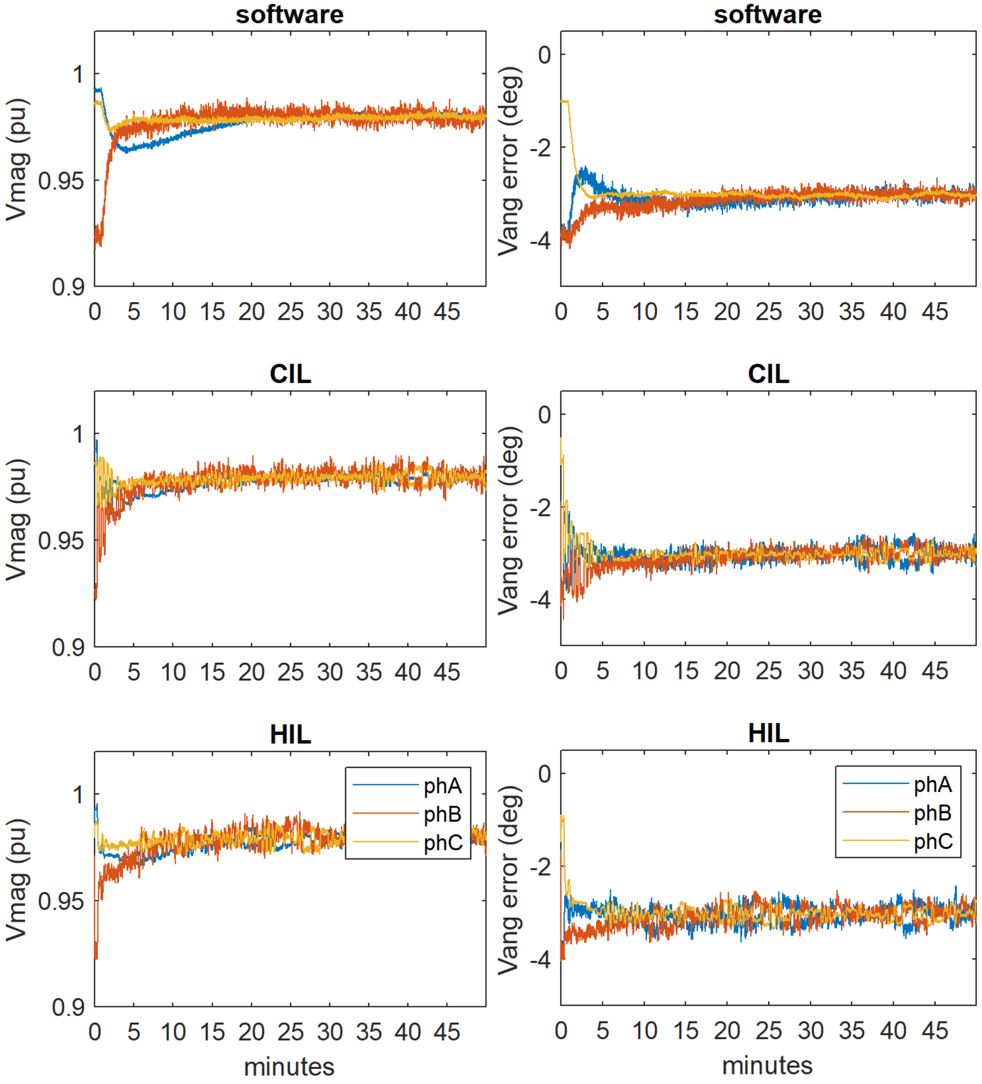

Figure 4.7: Comparison of voltage magnitude and phase angle between software, CIL, and HIL tests on the 344NFunbal

In Fig. 4.7 We compare the performance of the PI controllers between software, CIL, and HIL tests by plotting the voltage magnitude and phase angle at the performance node. All three tests successfully track the phasor target on this large feeder. Our previous work [39] exhibited challenges with coupling between real and reactive power actuation and A/B/C phase coupling when simulating on large feeders. Hence it is notable that our designed controllers overcome the coupling affects in all three testing modes, resulting in good tracking of the phasor target with minimal steady-state error.

4.3 Conclusion

In this work we implemented the Phasor-Based Control framework on real hardware at LBNL. The test setup is successful in coordinating multiple DERs to execute real and reactive power commands for tracking μPMU measurements. In particular, the testbed includes smart inverters, a PV and battery system, controllable loads, and a μPMU. In creating the hardware implementation we overcame several practical challenges, including the rewiring of the original 3-phase connections from Delta to Wye configurations, and the creation of an advanced control mode to enable 4-quadrant inverter control. The test results exhibit effective phasor tracking, where PI-controlled actuators and load racks overcome second-wise solar PV variations and large load disturbances. By comparing the software simulations to CIL and HIL tests, we observe similarly effective performance, with reasonable differences in settling time and amount of noise.

Chapter 5

Placement of PBC actuators and sensors

This chapter is based on the paper "Visual Tool for Assessing Stability of DER Configurations on Three-Phase Radial Networks" [50], written in collaboration with Brittany Wais, Elizabeth Ratnam, and Alexandra von Meier.

5.1 Abstract

We present a method for evaluating the placement of Distributed Energy Resources (DER) on distribution circuits in order to control voltages and power flows. Our previous work described Phasor-Based Control (PBC), a novel control framework where DERs inject real and reactive power to track voltage magnitude and phase angle targets. Here, we employ linearized power flow equations and integral controllers to develop a linear state space model for PBC acting on a three-phase unbalanced network. We use this model to evaluate whether a given inverter-based DER configuration admits a stable set of controller gains, which cannot be done by analyzing controllability nor by using the Lyapunov equation. Instead, we sample over a parameter space to identify a stable set of controller gains. Our stability analysis requires only a line impedance model and does not entail simulating the system or solving an optimization problem. We incorporate this assessment into a publicly available visualization tool and demonstrate three processes for evaluating many control configurations on the IEEE 123-node test feeder (123NF).

5.2 Introduction

On distribution grids it is increasingly important to effectively control DERs, especially in order to address power quality issues introduced by uncontrolled solar resources. As more controllable DERs are installed, we must analyze whether these devices will co-operate as intended, or if they will exhibit adverse interactions. This coordination problem is not only determined by each DER's control strategy, but also their placement and communication setup.

Typically, the communication setup for inverter control is local, where inverters use measurements at their own node to modify their power output with the goal of regulating voltage and/or frequency. Yet simulations of local droop volt-var control (DVVC) inverters have indicated risks of oscillations [23, 40], reminding us that when coordinating groups of DERs it is critical to guarantee voltage stability. Additionally, there are opportunities for groups of electrically spaced inverters to collectively address voltage issues at nearby nodes.

PBC is a versatile framework for recruiting diverse DERs to support safe and resilient grid operations. Our team has previously presented the conceptual rationale for PBC [20] and demonstrated it with simulations [39] and with hardware [49]. In this work, we develop a state space model under the PBC control framework. The model setup can be useful for other power injection — voltage regulation setups, such as DVVC and volt-watt control.

Our tool is distinct from capacity maps, which are used to determine when uncontrollable solar PV violates voltage constraints with and without controllable DERs. In the hosting capacity analysis of [51], the configuration of controllable DERs is fixed, and the inverter control laws do not consider newer requirements for actuating both real and reactive power [13]. Yet the configuration and control law of controllable DERs has a significant impact on whether voltage violations occur [52] and should be considered. DER placement tools should consider those factors and also preserve the visual features of capacity maps to gain topological insights.

Our tool may also be compared to optimal power flow simulations. The approaches in [53, 54] compute optimal power dispatches for controllable DERs to achieve objectives, but require detailed setup and can be computationally expensive to solve. Furthermore, modeling assumptions made in the choice of lines, loads, and weather may limit the applicability of the simulation results. Rather than setup a detailed simulation, our tool quickly evaluates many controller configurations and only requires a feeder line impedance model. Because our tool does not simulate any system, we do not make claims about time-series performance, DER capacity limit violations, or power loss. Our tool focuses in investigating the stability of proposed control configurations, whose results can then inform the setup of a simulation if needed.

In this work we develop a novel linear state space model to analyze the network-wide stability of inverters that inject real and reactive power. To do so, we assume the dynamics of loads, lines, and inverters are much faster than the inverter power set-point control law [36, 38, 55]. The algebraic DistFlow equations and the proposed integrator controllers form a closed-loop quasi-steady state dynamical system. The proposed system is consistent with the model in [55], with an extension that incorporates the voltage phase angle. Finally, we incorporate this model into a tool that illustrates good locations to place controllable inverter-based DERs.

5.3 Problem Formulation

Example on IEEE 123-node Test Feeder

The Phasor-Based Control (PBC) framework involves sending real and reactive power set-point commands to controllable DERs at *actuator nodes* to drive the voltage magnitude and phase angle measured at designated *performance nodes* to computed optimal phasor targets. By achieving these targets, we meet supervisory-level objectives such as reducing voltage volatility, balancing the three phases, and preventing reverse power flow.

We motivate this work by way of an example on the 123NF [3]: let χ be an arbitrarily chosen controller configuration of co-located actuator and performance node pairs where PBC successfully drives convergence to the phasor targets. We create configuration C_1 by adding an actuator-performance node pair at node 61 to χ. In contrast, we create configuration C_2 by adding a pair to χ at node 60, which is adjacent to node 61. We design PBC controllers with C_1 and C_2 using the method from our previous work [39], and simulate the closed-loop systems using Opal-RT's ePHASORSIM nonlinear power flow simulator. In the simulation we use reasonable phasor targets and initial conditions, and apply three step change power disturbances.

As shown in Fig. 5.2, the voltage magnitude tracking errors of C_2 do not converge to zero. In contrast, the voltage magnitude tracking errors of C_1 in Fig. 5.1 converge after 350 seconds to $\leq$0.2%, which is equal to five volts. Note that before the simulation, it was not intuitive whether either configuration would converge. Furthermore, it is not obvious why C_1 converges but C_2 does not. Our tool can determine, without simulating the scenario, whether a set of controller gains exists that will ensure tracking convergence for any given controller configuration. In our results section we return to this example and employ our tool to provide insight on the differing convergence behavior.

State Space Model Derivation

Voltage Magnitude Equation

Consider the Distflow [26] branch equation for a single-phase radial network

$$|V_i|^2 - |V_j|^2 = 2(r_{ij}P_{ij} + x_{ij}Q_{ij}) + (r_{ij}^2 + x_{ij}^2)\frac{(P_{ij}^2 + Q_{ij}^2)}{|V_i|^2}, \tag{5.1}$$

which approximates the relationship between voltage magnitudes V_i, V_j and power flow $P_{ij} + \mathbf{j}Q_{ij}$ from node i to node j with complex impedance $r_{ij} + \mathbf{j}x_{ij}$.

We linearize equation (5.1) about a nominal voltage of $1p.u.$ by dropping the square term. Next, let v_i be the squared voltage magnitude, p_i the net real power, q_i the net reactive power at node i, and define vectors $v = [v_1, v_2, ...v_n]^T$, $p = [p_1, p_2, ...p_n]^T$, $q = [q_1, q_2, ...q_n]^T$,$v_0 = [v_0, v_0, ...v_0]^T$ on a network with n nodes. Here v_0 refers to the substation node which is constant at $1p.u.$. As done in [36, 38, 55], we choose time step k to be sufficiently large

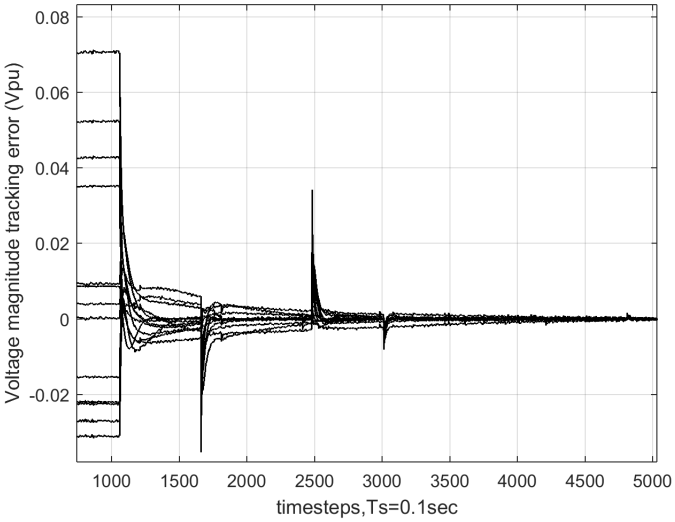

Figure 5.1: Voltage magnitude tracking error failing to converge when configuration C_1 is simulated on the 123NF

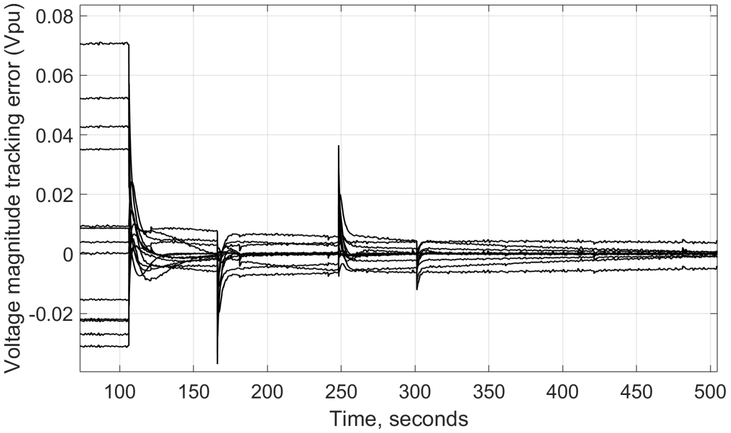

Figure 5.2: Voltage magnitude tracking error failing to converge when configuration C_2 is simulated on the 123NF

enough for the dynamics from inverters, lines, and loads to settle to steady state before new power injections are updated. The algebraic relationship between nodal power injections and squared nodal voltages at all nodes for time steps k and $k+1$ becomes

$$v_k = Rp_k + Xq_k + v_0 \tag{5.2}$$

$$v_{k+1} = Rp_{k+1} + Xq_{k+1} + v_0 \tag{5.3}$$

where the entries of matrices R and X at the i^{th} row and j^{th} column are given by

$$R_{ij} = 2 \sum_{(h,k)\in\mathcal{P}_i\cap\mathcal{P}_j} r_{hk} \tag{5.4}$$

$$X_{ij} = 2 \sum_{(h,k)\in\mathcal{P}_i\cap\mathcal{P}_j} x_{hk}. \tag{5.5}$$

$\mathcal{P}_i$ is the unique set of lines (or path) connecting node i back to the substation node.

We subtract equation (5.2) from (5.3), giving

$$v_{k+1} = v_k + R(p_{k+1} - p_k) + X(q_{k+1} - q_k). \tag{5.6}$$

To extend equation (5.6) to a three-phase system we consider each phase as a separate node and triple the set of n nodes as done in [38, Appendix]. Each vector element in equation (5.6) is replaced with a 3x1 vector, and each element of matrices R and X is replaced with a 3x3 block matrix. This gives $v, p, q \in \mathcal{R}^{3n\times1}$ and $R, X \in \mathcal{R}^{3n\times3n}$.

Because we typically seek to drive voltage magnitudes to $1p.u.$ and balance phases to 120° apart, we define time-varying phasor targets with $v^{ref} \in \mathcal{R}^{3n}$ values near one, and $\delta^{ref} \in \mathcal{R}^{3n}$ values with a repeated sequence near $[0\ -120\ 120]^\top$. Subtracting v^{ref}_{k+1} from both sides of equation (5.6), we have

$$v_{k+1} - v^{ref}_{k+1} = (v_k - v^{ref}_k) + (v^{ref}_k - v^{ref}_{k+1}) + R(p_{k+1} - p_k) + X(q_{k+1} - q_k) \tag{5.7}$$

Voltage Phase Angle Equation

The relationship between nodal voltage phase angles δ_i, δ_j and power flow on a single-phase radial network is described by

$$\sin(\delta_i - \delta_j) = \frac{x_{ij}P_{ij} - r_{ij}Q_{ij}}{|V_i|\,|V_j|}. \tag{5.8}$$

To linearize the equation, we make the small-angle approximation $\sin\delta \approx \delta$ and assume $V_i \approx V_j \approx 1p.u.$, retaining the dependence of P_{ij} and Q_{ij} on $(\delta_i - \delta_j)$ [20].

In extension to all nodes, we define the vector $\delta = [\delta_1, \delta_2, ...\delta_n]^T$. Here δ_0 is a vector of the substation nodal voltage phase angle, which is constant at 0°. The algebraic relationship between nodal power injections and voltage phase angles at all nodes for time steps k and $k+1$ becomes

$$\delta_k = -\frac{1}{2}Rq_k + \frac{1}{2}Xp_k + \delta_0 \tag{5.9}$$

$$\delta_{k+1} = -\frac{1}{2}Rq_{k+1} + \frac{1}{2}Xp_{k+1} + \delta_0. \tag{5.10}$$

We subtract equation (5.9) from (5.10), giving

$$\delta_{k+1} = \delta_k - \frac{1}{2}R(q_{k+1} - q_k) + \frac{1}{2}X(p_{k+1} - p_k). \tag{5.11}$$

We extend equation (5.11) to a three-phase system in the same way as done in section 5.3. Then subtracting the phasor targets δ_{k+1}^{ref} from both sides gives

$$\delta_{k+1} - \delta_{k+1}^{ref} = (\delta_k - \delta_k^{ref}) + (\delta_k^{ref} - \delta_{k+1}^{ref}) - \frac{1}{2}R(q_{k+1} - q_k) + \frac{1}{2}X(p_{k+1} - p_k). \tag{5.12}$$

Nodal Power Update Equations

The update equation for net nodal powers at time step k

$$q_k = q_k^{inv} + q_k^{other} \tag{5.13}$$

$$p_k = p_k^{inv} + p_k^{other}, \tag{5.14}$$

where (q^{inv}, p^{inv}) are inverter set-point power commands and (q^{other}, p^{other}) are power injections from load and generation sources that are not under our control. We consider these power update equations at time step $k + 1$, then substitute these four equations into (5.7) and (5.12), giving

$$\begin{aligned} v_{k+1} - v_{k+1}^{ref} = (v_k - v_k^{ref}) + (v_k^{ref} - v_{k+1}^{ref}) + R(p_{k+1}^{inv} - p_k^{inv}) + R(p_{k+1}^{other} - p_k^{other}) + \\ X(q_{k+1}^{inv} - q_k^{inv}) + X(q_{k+1}^{other} - q_k^{other}), \end{aligned} \tag{5.15}$$

$$\begin{aligned} \delta_{k+1} - \delta_{k+1}^{ref} = (\delta_k - \delta_k^{ref}) + (\delta_k^{ref} - \delta_{k+1}^{ref}) - \frac{1}{2}R(q_{k+1}^{inv} - q_k^{inv}) - \frac{1}{2}R(q_{k+1}^{other} - q_k^{other}) + \\ \frac{1}{2}X(p_{k+1}^{inv} - p_k^{inv}) + \frac{1}{2}X(p_{k+1}^{other} - p_k^{other}). \end{aligned} \tag{5.16}$$

Inverter Control Law

We design our controller set-point update strategy as a discrete-time integrator with gain matrices F_{11}, F_{12}, F_{21}, and F_{22}, where

$$q_{k+1}^{inv} - q_k^{inv} = -F_{11}(v_k - v_k^{ref}) - F_{12}(\delta_k - \delta_k^{ref}), \tag{5.17}$$

$$p_{k+1}^{inv} - p_k^{inv} = -F^{21}(v_k - v_k^{ref}) - F_{22}(\delta_k - \delta_k^{ref}). \tag{5.18}$$

The inverter power injection will decrease when the voltage is too high $(v_k - v_k^{ref}) > 0$ and increase when voltage is too low. Equation (5.17) differs from the analogous DVVC law, $q_{k+1}^{inv} = -F_{11}(v_k - v_k^{ref})$. Specifically, we map the tracking error to the next *change in actuation* command, in contrast to how DVVC maps it to the next actuation command.

Quasi-steady State Dynamical System

Let our states be the voltage magnitude tracking error $e^v = v - v^{ref}$ and voltage phase angle tracking error $e^\delta = \delta - \delta^{ref}$. We define our inputs be the change in inverter actuation $u^q_k = q^{inv}_{k+1} - q^{inv}_k$, $u^p_k = p^{inv}_{k+1} - p^{inv}_k$. After substituting (5.17) and (5.18) into (5.15) and (5.16), our state space equations are

$$\begin{bmatrix} e^v_{k+1} \\ e^\delta_{k+1} \end{bmatrix} = A \begin{bmatrix} e^v_k \\ e^\delta_k \end{bmatrix} + B \begin{bmatrix} u^q_k \\ u^p_k \end{bmatrix} + \begin{bmatrix} c^q_k \\ c^p_k \end{bmatrix} + \begin{bmatrix} d^q_k \\ d^p_k \end{bmatrix}, \tag{5.19}$$

$$\begin{bmatrix} u^q_k \\ u^p_k \end{bmatrix} = -F \begin{bmatrix} e^v_k \\ e^\delta_k \end{bmatrix}, \tag{5.20}$$

$$A = \begin{bmatrix} I & 0 \\ 0 & I \end{bmatrix}, B = \begin{bmatrix} X & R \\ -\frac{1}{2}R & \frac{1}{2}X \end{bmatrix}, F = \begin{bmatrix} F_{11} & F_{12} \\ F_{21} & F_{22} \end{bmatrix}, \tag{5.21}$$

where $c^v_k = (v^{ref}_k - v^{ref}_{k+1})$, and $d^q_k = R(p^{other}_{k+1} - p^{other}_k) + X(q^{other}_{k+1} - q^{other}_k)$, which are the changes in voltage magnitude targets and changes in voltage magnitude from uncontrollable sources, respectively. Likewise, $c^\delta_k = (\delta^{ref}_k - \delta^{ref}_{k+1})$, and $d^p_k = \frac{1}{2}X(p^{other}_{k+1} - p^{other}_k) - \frac{1}{2}R(q^{other}_{k+1} - q^{other}_k)$. Note that c^q_k, c^p_k, d^q_k, and d^p_k are time-varying terms that are independent of the state. The authors in [55] formulate a similar open loop and feedback control equations, but only for reactive power driving voltage magnitudes to the nominal $V = 1p.u.$ on single-phase networks. Our use of power injections to track voltage phase angle targets is novel as well as critical to the PBC framework.

Disturbance Model

After substituting the feedback law (5.20) into (5.19), we have $x_{k+1} = (A - BF)x_k + c_k + d_k$.

Power disturbances from uncontrollable sources such as load changes, cloud cover events, and solar PV fluctuations can cause voltage spikes resulting in unintended device tripping. We model these disturbances with time-series profiles as done in [38, 55]. Modeled this way, disturbances d_k and phasor targets c_k do not change the eigenvalues of A_{cl}. To evaluate stability of the closed-loop system, we set $c_k = d_k = 0$, giving

$$x_{k+1} = (A - BF)x_k = A_{cl}x_k. \tag{5.22}$$

Eq. (5.22) is a linear time-invariant (LTI) system with dynamic elements arising from integral control action.

In what follows we design F so that the system $x_{k+1} = A_{cl}x_k + c_k + d_k$ operates close to the equilibrium of $V = 1pu$. In more detail, we assume the phasor target changes c_k, voltage disturbances d_k, and initial conditions are small, such that the open-loop system (5.19) operates close to our linearization equilibrium of $V = 1pu$.

How Configurations Inform Gain Matrix Requirements

Communication setups of controllable DERs and sensors on real grids directly determine sparsity requirements on the controller gain matrix F. For a three-phase grid network with n nodes, F has dimension $6n \times 6n$.

In F_{11}, F_{12}, F_{21}, and F_{22}, there is an arrangement of n^2 3x3 blocks, each one representing a node with up to three phases. If an actuator on node i is actuating to track the phasor target at node j, there is a nonzero 3x3 block at the (i,j) location of F_{11}, F_{12}, F_{21}, and F_{22}.

If in our control law, reactive power commands are computed as a function of voltage magnitude and not phase angle, $F_{12} = 0$. Similarly, if real power commands are computed as a function of phase angle and not voltage magnitude, $F_{21} = 0$. If power commands on one phase are computed from only that phase's measurements, then all 3x3 blocks are diagonal.

Considering realistic scenarios of the PBC framework, we make the following assumptions when designing F.

Assumption 1. *each actuator is used to track a single phasor target. As a result, every row of F can only have up to one non-zero element.*

Assumption 2. $F_{12} = F_{21} = 0$*, and the 3x3 blocks representing three-phase nodes in* F_{11} *and* F_{22} *are diagonal.*

An example configuration that satisfies assumptions 1 and 2 is shown in Fig. 5.3. The actuator at node 4 tracks the voltage phasor at its own node, while actuators at node 1 and 3 track the voltage phasor at node 2. The controller gain matrix F associated with this setup is (5.23) where D_{3x3} are diagonal matrices containing the actuator controller gains.

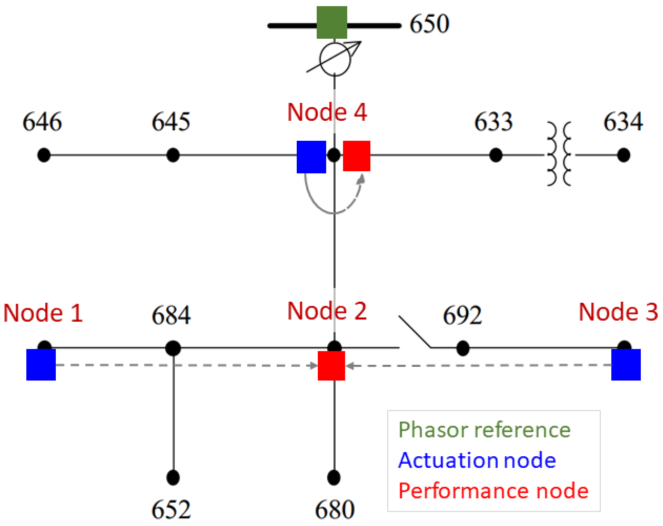

Figure 5.3: Diagram of multiple performance nodes with colocated and non-colocated actuators on the IEEE 13-node feeder [3]

$$F = \begin{bmatrix} 0 & D_{3x3} & 0 & 0 & 0 & 0 & 0 & 0 \\ 0 & 0 & 0 & 0 & 0 & 0 & 0 & 0 \\ 0 & D_{3x3} & 0 & 0 & 0 & 0 & 0 & 0 \\ 0 & 0 & 0 & D_{3x3} & 0 & 0 & 0 & 0 \\ 0 & 0 & 0 & 0 & 0 & D_{3x3} & 0 & 0 \\ 0 & 0 & 0 & 0 & 0 & 0 & 0 & 0 \\ 0 & 0 & 0 & 0 & 0 & D_{3x3} & 0 & 0 \\ 0 & 0 & 0 & 0 & 0 & 0 & 0 & D_{3x3} \end{bmatrix} \tag{5.23}$$

Let the subspace W encapsulate all sparsity structure requirements on matrix F. Let I_W be the structural identity of the subspace S, with its ij^{th} entry defined as

$$[I_W]_{ij} = \begin{cases} 1, & \text{if} \quad F_{ij} \quad \text{is a free variable;} \\ 0, & \text{if} \quad F_{ij} = 0 \quad \text{is required.} \end{cases} \tag{5.24}$$

We seek an $F \in W$ that drives (5.22) to be closed-loop stable.

Applicability of Controllability

One may seek to assess controllability of (A, B) from (5.19). If (A, B) is controllable, there exists an F matrix of *any* sparsity structure that makes (5.22) stable. F could be totally dense, which corresponds to an unrealistic communication setup where there is a controllable actuator at *every* node, and each one has access to sensor measurements at *every* node. Realistic communication setups are likely to impose sparsity requirements, such as those in Assumption 1. For example, in DVVC inverters, where inverters actuate reactive power to regulate the voltage magnitude their own nodes, the F matrix would require F_{11} to be diagonal and $F_{12} = F_{21} = F_{22} = 0$. Therefore, controllability of (5.19) is not generally sufficient for determining the convergence of realistic configurations of actuators.

Conditions for Stability

We use $|.|$ as the cardinality operator on sets. Let $M(i,:)$ denote the i^{th} row, and $M(:,i)$ the i^{th} column of a matrix M . If i is a set of indices then $M(i,:)$ and $M(:,i)$ represent the rows and columns at those indices, respectively.

A discrete LTI system $x_{k+1} = Mx_k$ is said to be *stable in the sense of Lyapunov* (SISL) if x_k is bounded for all time $k \geq k_0$. If the eigenvalues of M are on or in the unit circle, and those on the unit circle have 1x1 Jordan blocks, the system is SISL [56, Chapter 5.3]. If any Jordan blocks associated with eigenvalues on the unit circle are larger than size $1x1$, the upper diagonal terms will grow at polynomial rate to infinity, causing instability of one or more states. It is computationally expensive to compute the Jordan canonical form of a matrix. Instead, we leverage the property that the number of Jordan blocks associated with an eigenvalue λ of M is equal to the nullity of $(M - \lambda I)$. If the multiplicity of λ is equal to this nullity, all associated Jordan blocks are 1x1. Let U be each distinct set of eigenvalues on the unit circle.

Theorem 1. *If*

1. $abs(\lambda) \leq 1 \quad \forall \lambda \in eig(M)$
2. $nullity(M - \lambda I) = |U| \quad \forall \lambda \in U$

then the system $x_{k+1} = Mx_k$ *is stable in the sense of Lyapunov.*

Stability Yields Phasor Tracking

We now prove that if (5.22) satisfies Theorem 1, the inverters will drive the performance node voltages to their phasor targets. Consider the phasor tracking error $x \in \mathcal{R}^{3n}$ from (5.22). Let p be the indices of x that we want to drive to zero. Let $\bar{p}$ be the remaining indices of x. Note that $|p| + |\bar{p}| = n$.

Proposition 1. *Consider a gain matrix F defined in* (5.20) *whose columns at indices p are not the zero vector ($F(:,p) \neq 0$). If F is designed so that* (5.22) *satisfies Theorem 1, the p-indexed states $x(p)$ will be driven zero.*

The state vector of (5.22) can be written with Jordan canonical form as

$$x_k = A_{cl}^k x_0 = TJ^kT^{-1}x_0. \tag{5.25}$$

The right eigenvectors of A_{cl} , e_i, make up the columns of T, the transpose of the left eigenvectors v_i make up the rows of T^{-1}, and J is the Jordan block matrix of A_{cl} [57]. Let U denote the set of eigenvalues at one, and let S denote those inside the unit circle. Because the open-loop system in (5.19) has all eigenvalues equal to one, a SISL closed-loop system in (5.22) will have eigenvalues in U or in S.

The expansion of x_k into eigenvalue terms is

$$x_k = \sum_{i \in S} \tilde{E}_i \tilde{\Pi}_i^k \tilde{V}_i^T x_0 + \sum_{i \in U} E_j \Pi_j^k V_j^T x_0, \tag{5.26}$$

$$= \sum_{i \in S} s_{i,k} + \sum_{j \in U} u_{j,k}, \tag{5.27}$$

where E_j ($\tilde{E}_i$) is constructed by selecting the submatrix of T associated with the j^{th} (i^{th}) eigenvalue, then zero-padding the submatrix to obtain the same dimensions as T. In the same way, V_j ($\tilde{V}_i$) constructed from T^{-1}, and Π_j^k ($\tilde{\Pi}_i^k$) is constructed from J^k. Details of this construction can be found in [57, Chapter 4.4]. We denote $u_{j,k}$ ($s_{i,k}$) as the j^{th} (i^{th}) term associated with eigenvalues equal to one (in the unit circle).

Lemma 1. *If the closed-loop system* (5.22) *is designed to satisfy Theorem 1,* $F(:,p) \neq 0 \implies E_j(p,:) = 0 \quad \forall j \in U$.

Proof of Lemma 1

Consider matrices A, B, F for the system in (5.22). The eigenvector equation for the j^{th} one eigenvalue of A_{cl} in U is $(A_{cl} - 1 \cdot I)e_j = 0$. Because $A = I$, this becomes $(I - BF - I)e_j = 0$, which simplifies to $-BFe_j = 0$.

Next we show that B, which is constructed from R and X matrices in (5.19), is invertible. By definition $X \succ 0$ and $R \succ 0$ [36]. From properties of positive definite matrices, $\frac{1}{2}X - (-\frac{1}{2}R^T)X^{-1}R \succ 0$. This is useful because $det(B) = det(X) \cdot det(\frac{1}{2}X - (-\frac{1}{2}R^T)X^{-1}R)$. Thus $det(B) \neq 0 \Leftrightarrow$ B is invertible.

Because B is invertible, $\mathcal{N}(B)$ is trivial, so $-BFe_j = 0 \implies Fe_j = 0$. Next we construct $\tilde{F}$ and $\tilde{e_j}$ by rearranging the columns and components of F and e_j respectively:

$$\tilde{F} = \begin{bmatrix} F(:,p) & F(:,\bar{p}) \end{bmatrix}, \; \tilde{e_j} = \begin{bmatrix} e_j(p) & e_j(\bar{p}) \end{bmatrix}^T \tag{5.28}$$

Note $\bar{p}$ are the indices of states that are not tracked, so $F(:,\bar{p}) = 0$. Thus, $Fe_j = \tilde{F}\tilde{e_j} = F(:,p) \cdot e_j(p)$. Assumption 1 implies that the p-index columns of F are linearly independent, so $\mathcal{N}(F(:,p))$ is trivial. This gives $F(:,p) \cdot e_j(p) = 0 \implies e_j(p) = 0$. E_j is constructed from the column vectors e_j, so $e_j(p) = 0 \implies E_j(p,:) = 0$

Proof of Proposition 1

Over time $\tilde{\Pi}_i^k \to 0$, causing $s_{i,k} \to 0$. In general the marginally stable eigenvalue terms $u_{j,k}$ contribute a constant value to all states, preventing any state from approaching zero. However, by Lemma 1, $E_j(p,:) = 0 \quad \forall j \in U$. Therefore $u_{j,k}(p) = 0 \quad \forall k \geq 0$. Together with $s_i^k \to 0$, $x_k(p) \to 0$.

Existence of Viable Controllers

The Existence Problem

One can determine whether there exists an unconstrained F matrix that satisfies the Lyapunov equation by solving a convex semi-definite program (SDP) [58, Chapter 4.4]. However, determining whether there exists an $F \in W$ that satisfies the lyapunov equation is a harder problem, and is sometimes setup as the static output feedback (SOF) stabilization problem [59–61]. This problem is a nonlinear (bilinear) SDP problem that is NP-hard [60]. Because few nonlinear SDP solvers produce reliable results for scaling system sizes, we instead sample candidate F matrices in a parameter space for our tool.

Sampling F matrices

For a given configuration if we can find at least one $F \in W$ such that $x_{k+1} = A_{cl}x_k$ satisfies Theorem 1, we call the configuration and associated F matrix *good*. Searching for good F's can never be exhaustive, so a *poor* configuration is one where we did not find a suitable F.

We now define a parameter space to meet design Assumptions 1 and 2. Within each of F_{11}, F_{12}, F_{21}, and F_{22} we choose all non-zero gain elements to be equal positive values f. From experience, when all gain elements are non-negative, F matrices with positive elements near the origin tend to be good. Hence we define the parameter space as a positive cone around the origin:

$$[F_{11}]_{ij}, [F_{21}]_{ij} = \begin{cases} 0, & \text{if} \quad [I_W]_{ij} = 0 \\ f_q \in [0, F_{ub}^q], & \quad otherwise, \end{cases} \tag{5.29}$$

$$[F_{12}]_{ij}, [F_{22}]_{ij} = \begin{cases} 0, & \text{if} \quad [I_W]_{ij} = 0 \\ f_p \in [0, F_{ub}^p], & \quad otherwise, \end{cases} \tag{5.30}$$

where $F_{ub}^q = (1/q)$ and $F_{ub}^p = (1/p)$ is computed once for each configuration. We compute q (p) as a heuristic estimate of the ratio of reactive power (real power) change at the actuation node to voltage magnitude (voltage phase angle) change at the associated performance node, averaged across all actuator-performance node pairs in the configuration.

5.4 Results

The procedure in Section 5.3 allows us to determine the stability of any configuration of actuator-performance node pairs (APNPs). We now present three processes of our tool that exercise this stability assessment on the 123NF, noting that the tool has also been implemented on a 344-node feeder. For all configurations we adopt Assumptions 1 and 2, then change the locations of APNPs to enforce different structural requirements on F per configuration. An APNP is *co-located* if an actuator and performance node are at the same location, and *non-colocated* otherwise.

Figures and code associated the following results can be downloaded at: `https://github.com/jaimiosyncrasy/heatMap`.

Non-colocated Placement Process (NPP)

The NPP is useful when users cannot place controllable DERs at the same locations as problematic voltages. Additionally, there can be value in coordinating multiple actuators at different nodes to track the same voltage at another node.

The NPP can be applied to a grid with any number of existing APNPs. We choose a candidate performance node location, then iterate through every other empty node in the feeder, fixing each as the associated candidate actuator node. Then, we generate a heatmap of the network, where a node's color indicates the stability of the configuration created by appending the candidate APNP to the existing set of APNPs. If the node is blue, several (at least 7% of) F matrices sampled from the parameter space defined in Section 5.3 were found that make the closed-loop system (5.22) satisfy Theorem 1. If the node is yellow, only a few (less than 7%) were found, and if red, no F matrices were found. Next we select a blue or yellow APNP to become part of the core configuration, and this chosen APNP is colored grey on subsequent heatmaps. We repeat this process until the desired number of APNPs have been placed. The NPP produces a stable configuration of APNPs in desired locations, and setp-by-step heatmaps show how the choice of performance node and placed APNPs affect the stability of placing the next APNP.

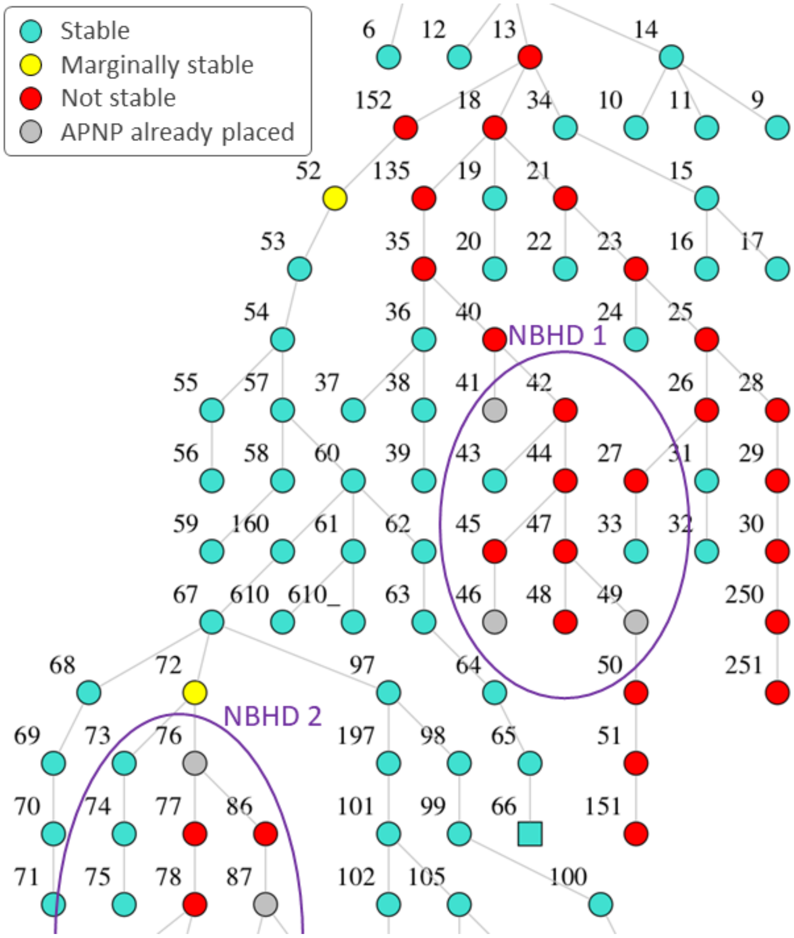

Figure 5.4: Heatmap generated by the NPP indicating good locations for placing a seventh actuator for tracking the voltage phasor at node 66 on the 123NF.

Neighborhood Scenario

We demonstrate the NPP on a feeder where there are two neighborhoods of existing APNPs. Specifically, a group of actuators located at node 41, 46, and 49 track the voltage phasor at node 44, and a group of actuators at node 76, 82, and 87 track the voltage phasor at node

Table 5.1: Best branches on the 123NF from running the NPP on the Neighborhood Scenario.

Branch start and end node	Percent stable	branch length (no. nodes)
node_68-node_71	100	4
node_109-node_114	100	5
node_197-node_350	100	6
node_152-node_66	98.7	11
node_160-node_451	98.2	8

77. In total there is an existing configuration of six APNPs. We run the NPP to find good locations for placing a seventh APNP, which will start a new group of actuators for tracking the voltage phasor at the chosen performance node (node 66). As shown in the heatmap of Fig. 5.4, locations near node 66 (marked with square), while locations near the existing two neighborhoods of actuators are more yellow and red. Notably, there is a color gradient between performance node 66 and performance node 44, but predicting the location of this color transition without the heatmap is not intuitive.

We validate the heatmap colors at nodes 152, 54, 67, 72, 84, and 18 from Fig. 5.4 using ePHASORsim. For blue and yellow nodes, we use the associated stable F matrices to simulate the closed-loop system (5.22) on the nonlinear grid model, and verify that the system converges to the phasor target. For red nodes, we use a more advanced but slower parameter search algorithm from [39] than our method in Section 5.3. All but one of the nodes checked by ePHASORSIM agree with the NPP results. Node 152 should be yellow and not red, indicating that our tool errs on the conservative side for borderline yellow-red cases.

Branch Analysis

Data collected across steps of the NPP can indicate good feeder branches to place APNPs. Let S be the set of 348 stable configurations found by the NPP when placing one to seven APNPs in the above neighborhood scenario. We call a network branch *used* each time at least one actuator from a stable configuration in S is located on that branch. Then for each branch, we compute the percentage of times it is used out of the total number of configurations involving the branch. This metric captures the branches that are the *most blue* across the NPP heatmaps. Table 5.1 lists the five branches with the highest percentage metric among the branches with length of at least four nodes. The best branches are located in the region between neighborhood groups one and two.

Table 5.2: Last four APNPs before all nodes unstable from six trials of running the auto-CPP.

seed	total placed	nodal distance to substation for last four APNPs (fourth-last, third-last, second-last, last)
6	11	1, 4, 13, 12
5	12	16, 10, 11, 4
2	13	16, 10, 3, 2
8	25	9, 17, 19, 4
4	27	16, 12, 2, 5
3	34	14, 5, 2, 2

Co-located Placement Process (CPP)

We randomly choose a node with no APNP, and if adding a co-located APNP there maintains a stable configuration, we place it there. We repeat this until our random choice yields an unstable configuration. We generate a heatmap with the same color key as the NPP that shows the stability of the configuration that would result from adding a co-located APNP at each of the remaining feeder nodes.

Running the CPP with a random seed of 3 generates the same configuration as χ from section 5.3, as shown in the heatmap of Fig. 5.5. We define the feeder's *main branch* to be the path from the edge node to the substation that has the most nodes branching from the path. The main branch of the 123NF is node_1-node_96. We observe from the CPP heatmap that this branch has many red and yellow nodes compared to other branches, indicating that it is better to place co-located actuators away from the main branch. Notably, node 60 is on the main branch, while node 61 is not, which may indicate why C_1 converged but C_2 did not in section 5.3.

Auto Co-located Placement Process (Auto CPP)

We randomly choose a node with no APNP, and if adding a co-located APNP there maintains a stable configuration, we place it there. In contrast to the non-auto CPP, when our random choice of location yields an unstable configuration, instead of stopping and producing a heatmap we continue to randomly sample the remaining nodes until we find a stable APNP. This algorithm finished when there are no remaining nodes that would maintain a stable configuration.

We run the auto CPP for six random seed trials, and compare the configurations of each trial in Table 5.2. We observe that the total number of APNPs placed varies significantly. Table 5.2 also lists the nodal distance to the substation of the last four co-located APNPs placed before all nodes were unstable. Given that the farthest nodal distance possible is 22

Table 5.3: Topology information about APNPs placed, from six trials of running the auto-CPP.

seed	total placed	number on or one-node-from edge	number at fork	number in middle	Percent on or one-node-from edge
6	11	4	3	4	36.4
5	12	8	2	2	66.7
2	13	8	2	3	61.5
8	25	17	3	5	68.0
4	27	16	6	5	59.3
3	34	24	6	4	70.6

nodes, we observe that the last APNPs are close to the substation, with the exception of the seed 6 trial.

For each run of the auto CPP we tally the number of APNPs that were placed on or one-node away from an edge node, at a network fork, or in the middle of a branch. From Table 5.3, we observe that the trials with more total APNPs have a higher percentage of APNPs on edge nodes. Placing co-located APNPs at edge nodes may pose the least disruption to the existing configuration, thereby enabling the placement of additional co-located APNPs.

5.5 Conclusion

In this work we derive a state space model under the PBC framework. We describe why controllability and the Lyapunov equation are not sufficient methods to assess the stability of realistic controller communication setups. We show that if our closed-loop system is designed to be stable in the sense of Lyapunov, the voltages at chosen performance nodes are driven to their phasor targets. We then use the LTI model in a tool to evaluate configurations on the 123NF. For configurations in which inverters regulate voltage phasors at nodes other than their own, we observe that actuators should be spaced apart, and this spacing can be visualized with our tool's heatmaps. Results on the 123NF also indicate that it is good to place co-located actuator-performance node pairs on or near edge nodes, poor to place them on the main branch, and poor to place them near the substation.

In future work we will investigate the modeling of dynamics from lines and loads that have comparable timescales to the inverter set-point control law. We will also compare the design choice of Assumption 2 to other state feedback strategies such as volt-watt control. Finally, we will explore conditions on the controller gains to ensure the closed-loop system stays near the linearization equilibrium.

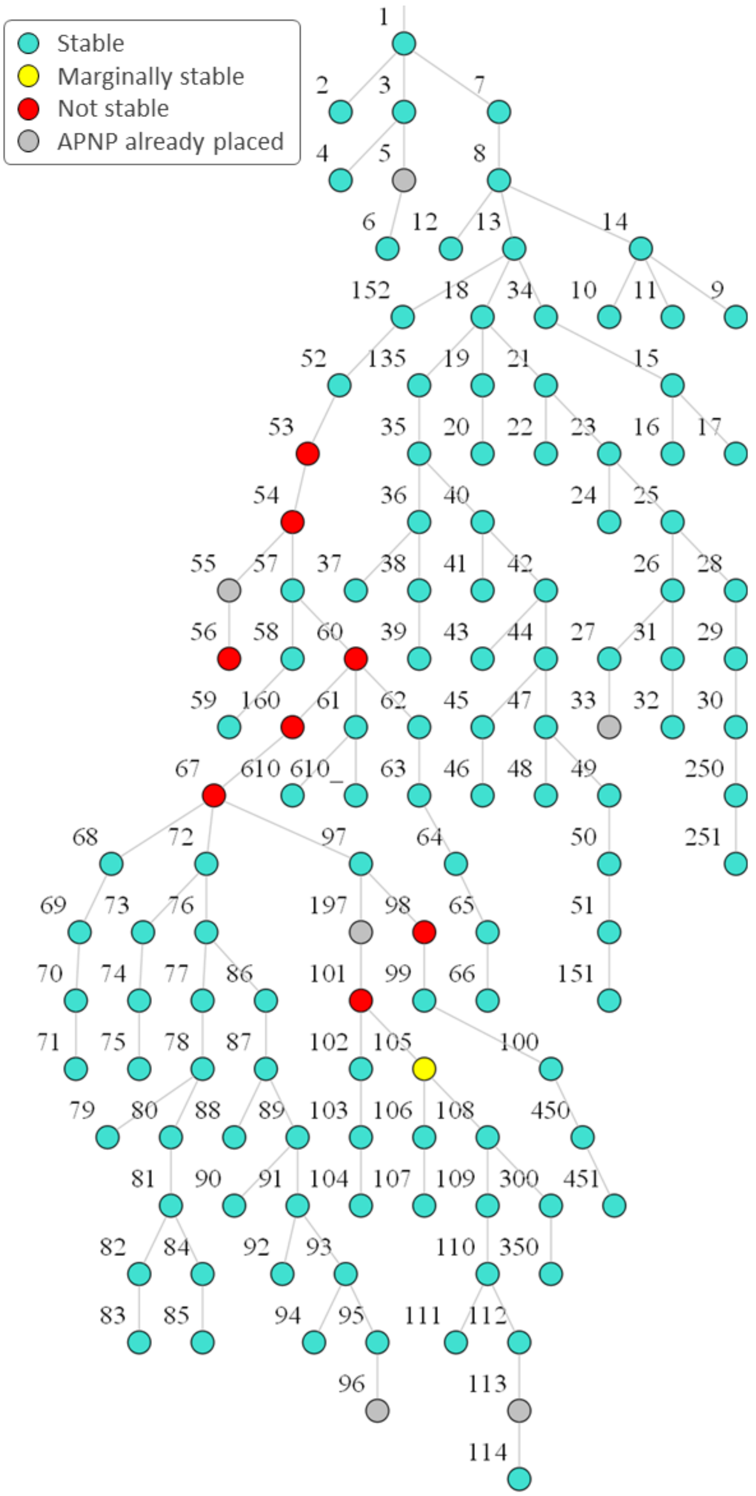

Figure 5.5: Heatmap generated by the CPP with a random seed of 3 on the 123NF, which results in the same configuration as χ from section 5.3.

Bibliography

[1] R. Rana, S. Sahoo, S. Mishra, and J. C. Peng, "Performance validation of cooperative controllers in autonomous ac microgrids under communication delay," in *2019 IEEE Power Energy Society General Meeting*, pp. 1–5, 2019.

[2] D. E. Seborg, *Multiloop and Multivariable Control*, ch. 18, p. 341–357. Hoboken, NJ, USA: Wiley, 3rd ed., 2011.

[3] *IEEE Distribution Test Feeders.* Available: http://sites.ieee.org/pes-testfeeders/resources/, Accessed 7 Nov. 2020.

[4] B. Mather, R. Seguin, J. Woyak, D. Costyk, and J. Hambrick, *High-Penetration PV Integration Handbook for Distribution Engineers.* Available: https://www.nrel.gov/grid/ieee-standard-1547/high-penetration-photovoltaic-integration-handbook.html, Accessed 14 Feb. 2021.

[5] J. Mead, V. Donde, and J. Garnett, *Advanced Control Technologies For Distribution Grid Voltage And Stability With Electric Vehicles And Distributed Generation.* Available: https://ww2.energy.ca.gov/publications/displayOneReport_cms.php?pubNum=CEC-500-2015-046, Accessed 14 Feb. 2021.

[6] Australian Energy Market Operator Limited, *Technical Integration of Distributed Energy Resources: Improving DER capabilities to benefit consumers and the power system. A report and consultation paper (2019).* Available: https://www.aemo.com.au/-/media/Files/Electricity/NEM/DER/2019/Technical-Integration/Technical-Integration-of-DER-Report.pdf, Accessed 14 Feb. 2021.

[7] K. Turitsyn, P. Šulc, S. Backhaus, and M. Chertkov, "Distributed control of reactive power flow in a radial distribution circuit with high photovoltaic penetration," in *IEEE PES General Meeting*, pp. 1–6, 2010.

[8] E. L. Ratnam, *Balancing distributor and customer benefits of battery storage co-located with solar PV.* Available: http://hdl.handle.net/1959.13/1312195, Accessed 11 May. 2019.

[9] Y. Xu, S. Çolak, E. C. Kara, S. J. Moura, and M. C. González, "Planning for electric vehicle needs by coupling charging profiles with urban mobility," *Nat. Energy*, vol. 3, no. 6, pp. 484–493, 2018.

[10] M. T. A. Kusko, *Power Quality in Electrical Systems.* Available: http://www.powerqualityworld.com/2011/04/ansi-c84-1-voltage-ratings-60-hertz.html, Accessed 14 Feb. 2021.

[11] Y. P. Agalgaonkar, B. C. Pal, and R. A. Jabr, "Distribution voltage control considering the impact of pv generation on tap changers and autonomous regulators," *IEEE Transactions on Power Systems*, vol. 29, no. 1, pp. 182–192, 2014.

[12] B. A. Robbins, C. N. Hadjicostis, and A. D. Domínguez-García, "A two-stage distributed architecture for voltage control in power distribution systems," *IEEE Transactions on Power Systems*, vol. 28, no. 2, pp. 1470–1482, 2013.

[13] "IEEE standard for interconnection and interoperability of distributed energy resources with associated electric power systems interfaces," *IEEE Std 1547-2018 (Revision of IEEE Std 1547-2003)*, 2018.

[14] G. Wenzel, M. Negrete-Pincetic, D. E. Olivares, J. MacDonald, and D. S. Callaway, "Real-time charging strategies for an electric vehicle aggregator to provide ancillary services," *IEEE Trans. Smart Grid*, vol. 9, pp. 5141–5151, Sep. 2018.

[15] D. M. Davies, M. G. Verde, O. Mnyshenko, Y. R. Chen, R. Rajeev, Y. S. Meng, and G. Elliott, "Combined economic and technological evaluation of battery energy storage for grid applications," *Nat. Energy*, vol. 4, no. 1, pp. 42–50, 2019.

[16] X. Chen, H. Zhang, Z. Xu, C. P. Nielsen, M. B. McElroy, and J. Lv, "Impacts of fleet types and charging modes for electric vehicles on emissions under different penetrations of wind power," *Nat. Energy*, vol. 3, no. 5, pp. 413–421, 2018.

[17] A. Parisio, E. Rikos, and L. Glielmo, "A model predictive control approach to microgrid operation optimization," *IEEE Transactions on Control Systems Technology*, vol. 22, no. 5, pp. 1813–1827, 2014.

[18] *PMUs and synchrophasor data flows in North America.* Available: https://www.naspi.org/node/387, Accessed 31 Dec. 2020.

[19] A. von Meier, E. Stewart, A. McEachern, M. Andersen, and L. Mehrmanesh, "Precision micro-synchrophasors for distribution systems: A summary of applications," *IEEE Transactions on Smart Grid*, vol. 8, pp. 2926–2936, Nov. 2017.

[20] A. von Meier, E. Ratnam, K. Brady, K. Moffat, and J. Swartz, "Phasor-based control for scalable integration of variable energy resources," *Energies*, vol. "13", p. "190", Jan 2020.

[21] J. M. Guerrero, J. C. Vasquez, J. Matas, L. G. de Vicuna, and M. Castilla, "Hierarchical control of droop-controlled ac and dc microgrids—a general approach toward standardization," *IEEE Transactions on Industrial Electronics*, vol. 58, no. 1, pp. 158–172, 2011.

[22] J. W. Simpson-Porco, Q. Shafiee, F. Dörfler, J. C. Vasquez, J. M. Guerrero, and F. Bullo, "Secondary frequency and voltage control of islanded microgrids via distributed averaging," *IEEE Transactions on Industrial Electronics*, vol. 62, no. 11, pp. 7025–7038, 2015.

[23] C. Lee, C. Chu, and P. Cheng, "A new droop control method for the autonomous operation of distributed energy resource interface converters," *IEEE Transactions on Power Electronics*, vol. 28, no. 4, pp. 1980–1993, 2013.

[24] J. Rocabert, A. Luna, F. Blaabjerg, and P. Rodríguez, "Control of power converters in ac microgrids," *IEEE Transactions on Power Electronics*, vol. 27, no. 11, pp. 4734–4749, 2012.

[25] D. Pattabiraman, R. H. Lasseter., and T. M. Jahns, "Comparison of grid following and grid forming control for a high inverter penetration power system," in *2018 IEEE Power and Energy Society General Meeting*, pp. 1–5, 2018.

[26] M. E. Baran and F. F. Wu, "Network reconfiguration in distribution systems for loss reduction and load balancing," *IEEE Trans. Power Del.*, vol. 4, pp. 1401–1407, Apr. 1989.

[27] P. Kundur, *Power System Stability and Control.* New York, NY, USA: McGraw-Hill, 3rd ed., 1994.

[28] H. Xu, A. D. Domínguez-García, V. V. Veeravalli, and P. W. Sauer, "Data-driven voltage regulation in radial power distribution systems," *IEEE Transactions on Power Systems*, vol. 35, no. 3, pp. 2133–2143, 2020.

[29] J. Zhang, Z. Chen, C. He, Z. Jiang, and L. Guan, "Data-driven-based optimization for power system var-voltage sequential control," *IEEE Transactions on Industrial Informatics*, vol. 15, no. 4, pp. 2136–2145, 2019.

[30] B. A. Mather, "Quasi-static time-series test feeder for pv integration analysis on distribution systems," in *2012 IEEE Power and Energy Society General Meeting*, pp. 1–8, 2012.

[31] N. Pogaku, M. Prodanovic, and T. C. Green, "Modeling, analysis and testing of autonomous operation of an inverter-based microgrid," *IEEE Transactions on Power Electronics*, vol. 22, no. 2, pp. 613–625, 2007.

[32] S. D'Arco, J. A. Suul, and O. B. Fosso, "Small-signal modelling and parametric sensitivity of a virtual synchronous machine," in *2014 Power Systems Computation Conference*, pp. 1–9, 2014.

[33] U. Markovic, O. Stanojev, E. Vrettos, P. Aristidou, and G. Hug, "Understanding stability of low-inertia systems," 02 2019.

[34] A. Singhal, V. Ajjarapu, J. Fuller, and J. Hansen, "Real-time local volt/var control under external disturbances with high PV penetration," *IEEE Transactions on Smart Grid*, vol. 10, pp. 3849–3859, Jul. 2019.

[35] P. Jahangiri and D. C. Aliprantis, "Distributed volt/var control by pv inverters," *IEEE Transactions on Power Systems*, vol. 28, pp. 3429–3439, Aug. 2013.

[36] M. Farivar, L. Chen, and S. Low, "Equilibrium and dynamics of local voltage control in distribution systems," in *52nd IEEE Conference on Decision and Control*, pp. 4329–4334, Dec. 2013.

[37] N. Li, G. Qu, and M. Dahleh, "Real-time decentralized voltage control in distribution networks," in *2014 52nd Annual Allerton Conference on Communication, Control, and Computing (Allerton)*, pp. 582–588, Sep. 2014.

[38] A. Eggli, S. Karagiannopoulos, S. Bolognani, and G. Hug, "Stability analysis and design of local control schemes in active distribution grids," *IEEE Trans. Power Syst.*, pp. 1–1, Sep. 2020.

[39] J. Swartz, E. Ratnam, T. Roberts, and A. von Meier, "Local phasor-based control of DER inverters for voltage regulation on distribution feeders," in *press, IEEE Green Technologies Conference*, Apr. 2020.

[40] S. Chakraborty, A. Hoke, and B. Lundstrom, "Evaluation of multiple inverter volt-var control interactions with realistic grid impedances," in *IEEE Power and Energy Society General Meeting*, Jul. 2015.

[41] D. B. Arnold, M. Negrete-Pincetic, M. D. Sankur, D. M. Auslander, and D. S. Callaway, "Model-free optimal control of var resources in distribution systems: An extremum seeking approach," *IEEE Transactions on Power Systems*, vol. 31, pp. 3583–3593, Sep. 2016.

[42] J. G. Ziegler and N. B. Nichols, "Optimum Settings for Automatic Controllers," *Journal of Dynamic Systems, Measurement, and Control*, vol. 115, pp. 220–222, 06 1993.

[43] W. L. Luyben, *Essentials of process control*. London, UK: McGraw-Hill, 1997.

[44] Q.-G. Wang, B. Zou, T.-H. Lee, and Q. Bi, "Auto-tuning of multivariable PID controllers from decentralized relay feedback," *Automatica*, pp. 319–330, Mar. 1997.

[45] F. Olivier, P. Aristidou, D. Ernst, and T. Van Cutsem, "Active management of low-voltage networks for mitigating overvoltages due to photovoltaic units," *IEEE Transactions on Smart Grid*, vol. 7, pp. 926–936, Mar. 2016.

[46] S. A. U. Islam, E. L. Ratnam, A. Goel, and D. S. Bernstein, "Phasor-based adaptive control of a test-feeder distribution network: Application of retrospective cost adaptive control to the IEEE 13-node test feeder," *IEEE Control Syst. Mag.*, vol. 39, pp. 56–74, Aug. 2019.

[47] H. Kervadec, J. Dolz, J. Yuan, C. Desrosiers, E. Granger, and I. B. Ayed, "Log-barrier constrained cnns," *Computing Research Repository (CoRR)*, vol. abs/1904.04205, 2019.

[48] M. Baudette, L. Chu, C. Gehbauer, K. Moffat, J. Pakshong, J. Swartz, and A. von Meier, "Hardware-in-the-loop benchmarking setup for phasor based control validation," in *preparation*, 2021.

[49] K. Moffat, J. Pakshong, L. Chu, G. Fierro, J. Swartz, M. Baudette, C. Gehbauer, and A. von Meier, "Phasor based control with the distributed extensible grid control platform," in *IEEE Innovative Smart Grid Technologies (ISGT)*, 2021.

[50] J. Swartz, B. Wais, E. Ratnam, and A. von Meier, "Visual tool for assessing stability of DER configurations on three-phase radial networks," *preprint arXiv:2011.07232, accepted to IEEE Powertech 2021*, Nov. 2020.

[51] J. Seuss, M. J. Reno, R. J. Broderick, and S. Grijalva, "Improving distribution network pv hosting capacity via smart inverter reactive power support," in *IEEE Power and Energy Society General Meeting*, pp. 1–5, Jul. 2015.

[52] H. Nazaripouya, Y. Wang, P. Chu, H. R. Pota, and R. Gadh, "Optimal sizing and placement of battery energy storage in distribution system based on solar size for voltage regulation," in *IEEE Power and Energy Society General Meeting*, pp. 1–5, Jul. 2015.

[53] F. Ding and B. Mather, "On distributed PV hosting capacity estimation, sensitivity study, and improvement," *IEEE Trans. Sustain. Energy*, vol. 8, pp. 1010–1020, Dec. 2017.

[54] M. Farivar, R. Neal, C. Clarke, and S. Low, "Optimal inverter VAR control in distribution systems with high PV penetration," in *2012 IEEE Power and Energy Society General Meeting*, pp. 1–7, Jul. 2012.

[55] R. E. Helou, D. Kalathil, and L. Xie, "Communication-free voltage regulation in distribution networks with deep PV penetration," in *Hawaii International Conference on System Sciences (HICSS)*, Jan. 2020.

[56] C.-T. Chen, *Linear System Theory and Design.* New York, NY, USA: Oxford University Press, Inc., 3rd ed., 1998.

[57] F. M. Callier and C. A. Desoer, *Linear System Theory.* Berlin, Heidelberg: Springer-Verlag, 1991.

[58] J. Zhang, A. Kumar, and S. K. Nguang, *Robust Observer-Based Fault Diagnosis for Nonlinear Systems Using MATLAB.* Appendix: Solving Linear Matrix Inequality (LMI) Problems, Springer, 2016.

[59] C. Kanzow, D. Steck, and D. Wachsmuth, “An augmented lagrangian method for optimization problems in banach spaces,” *SIAM Journal on Control and Optimization*, vol. 56, p. 272–291, Jan. 2018.

[60] Z. Cheng, J. Ma, X. Li, M. Tomizuka, and T. H. Lee, “Second-order non-convex optimization for constrained fixed-structure static output feedback controller synthesis,” *preprint arXiv:1912.04617*, Dec. 2019.

[61] J. Ma, S. Chen, N. Kamaldin, C. S. Teo, A. Tay, A. Al Mamun, and K. K. Tan, “Integrated mechatronic design in the flexure-linked dual-drive gantry by constrained linear–quadratic optimization,” *IEEE Transactions on Industrial Electronics*, vol. 65, no. 3, pp. 2408–2418, 2018.